

1

Snow Interception Relationships with 2 Meteorology and Canopy Density in a 3 Subalpine Forest

4

5 **Authors:**

6 Alex C. Cebulski¹ (ORCID ID - 0000-0001-7910-5056)

7 John W. Pomeroy¹ (ORCID ID - 0000-0002-4782-7457)

8 ¹Centre for Hydrology, University of Saskatchewan, Canmore, Canada

9 **Corresponding Author:** A.C. Cebulski, alex.cebulski@usask.ca

10 **Abstract:** Snow accumulation models differ in how snow interception and ablation processes
11 are represented and thus their application to diverse climates and forest types is uncertain.
12 Existing parameterisations of initial snow interception before unloading include inherently cou-
13 pled canopy snow accumulation and ablation processes. This leads to difficulty in diagnosing
14 processes and adding possible errors to simulations when incorporated as canopy interception
15 routines in models that already account for canopy snow ablation. This study evaluates the
16 theory underpinning parameterisations of initial snow interception using high-temporal reso-
17 lution and fine-scale measurements of throughfall for events with minimal snow ablation and
18 redistribution in both the canopy and on the ground. Relationships between these throughfall
19 measurements, event meteorology, and a novel lidar-based canopy density measurement were
20 assessed in two subalpine forest plots in the Canadian Rockies. Contrary to existing theories,
21 no association of canopy snow load or air temperature with interception efficiency was observed.

Instead, snow-leaf contact area emerged as the primary factor governing snow accumulation. A wind-driven snowfall event demonstrated that non-vertical hydrometeor trajectories can significantly increase snow-leaf contact area, thereby enhancing initial interception before ablation. Prediction of interception efficiency for this event was improved when adjusted for hydrometeor trajectory angle based on the wind speed at one-third of the canopy height. Snow-leaf contact area showed a high sensitivity to wind speed, increasing by up to 95% with a 1 m s^{-1} wind speed. The study proposes a new parameterisation that calculates throughfall, independent of processes that ablate snow from the canopy, as a function of snowfall, canopy cover, wind speed, and hydrometeor fall velocity. This new parameterisation successfully estimated sub-canopy snow accumulation for a snowfall event at two forest plots of differing canopy density and structure. By separating canopy snow ablation from snow interception processes, this new model offers potentially improved prediction of subcanopy snow accumulation when combined with canopy snow ablation parameterisations.

Keywords: snow interception, throughfall, ablation, forest, snowpack, lidar, process-based modelling

1 Introduction

Over half of North America's snow-covered zone is covered by forests (Kim et al., 2017), significantly impacting the accumulation and redistribution of snowpacks and subsequent snowmelt runoff. Essery et al. (2003) estimated that 25–45% of annual snowfall may be lost to the atmosphere due to sublimation of snow intercepted in forest canopies globally. Snow intercepted in the canopy can sublimate and melt at much higher rates than the subcanopy snowpack (Katsushima et al., 2023; Lundberg & Haldin, 1994; Pomeroy et al., 1998), reducing the amount of snow available for runoff. Canopy density is one of the primary factors controlling the partitioning of snowfall into throughfall and interception (Hedstrom & Pomeroy, 1998; Staines & Pomeroy, 2023) and thus governs the quantity of snow subject to sublimation from the canopy. Canopy structure metrics such as distance to canopy edge and total gap area have

48 also shown strong correlations to throughfall measurements at the event-based (Moeser et al.,
49 2015a) and seasonal (Mazzotti et al., 2019) timescales. Despite these relationships, forest thin-
50 ning efforts aimed at limiting sublimation losses to increase snowmelt runoff do not always
51 lead to a corresponding increase in spring streamflow (Golding & Swanson, 1978; Harpold et
52 al., 2020; Pomeroy et al., 2012; Troendle, 1983). This may be due to increased ablation rates
53 when forest cover is reduced, desynchronization of snowmelt timing, and sub-surface hydrology
54 interactions (Ellis et al., 2013; Musselman et al., 2015; Pomeroy et al., 1997; Safa et al., 2021;
55 Varhola et al., 2010). Given the significant impact of forest cover on snowpacks, along with the
56 limited or absent monitoring networks for subcanopy snow accumulation (Rittger et al., 2020;
57 Vionnet et al., 2021), land management, ecological conservation, and water resource decisions
58 depend on reliable models of snow redistribution.

59 Hedstrom & Pomeroy (1998), working in the cold continental boreal forest, proposed that ini-
60 tial snow interception efficiency was controlled by the maximum canopy load which itself was
61 a function of leaf area index and fresh snow density. Andreadis et al. (2009), incorporating
62 measurements from several studies (Kobayashi, 1987; Pfister & Schneebeli, 1999; Storck et al.,
63 2002), emphasized the role of leaf area index and air temperature in controlling the maximum
64 canopy snow load. Although these two parameterisations incorporate different processes and
65 relationships with air temperature, the Hedstrom & Pomeroy (1998) initial snow interception
66 parameterisation has shown strong performance at sites across Canada, Russia, Switzerland,
67 and Spain (Ellis et al., 2010; Gelfan et al., 2004; Pomeroy et al., 2022; Sanmiguel-Vallelado et
68 al., 2022), while the Andreadis et al. (2009) parameterisation has produced accurate results
69 in coastal environments (Andreadis et al., 2009; Clark et al., 2015). Subsequent research by
70 Lundquist et al. (2021) and Lumbrazo et al. (2022) has revealed overestimation of subcanopy
71 snow accumulation when combining the Hedstrom & Pomeroy (1998) routine with ablation
72 parameterisations from different studies (i.e., Roesch et al., 2001). The coupling of ablation pro-
73 cesses within existing snow interception parameterisations (Andreadis et al., 2009; Hedstrom
74 & Pomeroy, 1998) may contribute to overestimates of throughfall, canopy snow unloading, and
75 canopy snowmelt when combined with other canopy snow ablation parameterisations (Cebul-

ski & Pomeroy, 2025). Additional observations that separate initial snow interception from ablation processes could help determine the applicability of the interception theories proposed by Hedstrom & Pomeroy (1998) and Andreadis et al. (2009). Hedstrom & Pomeroy's (1998) theory also suggests that moderate wind speeds, which can result in more horizontal hydrometeor trajectories, increasing snow-leaf contact area and interception efficiency at the plot scale. This association has also been shown in rainfall interception studies to decrease throughfall of rain (Herwitz & Slye, 1995; Van Stan et al., 2011). However, the relationship proposed by Hedstrom & Pomeroy (1998), is typically not included in snow accumulation models as empirical testing of this relationship is lacking.

The objective of this paper is to evaluate the theories underlying existing snow interception models using high spatial and temporal resolution measurements of subcanopy snow accumulation for events with minimal canopy snow ablation. These new observations are investigated to address the following research questions:

1. Are the existing theories regarding the relationships between meteorology and canopy density and initial snow interception supported by in-situ observations collected in the Canadian Rockies?
2. How is initial snow interception influenced by non-vertical hydrometeor trajectory angles over a wind-driven snowfall event?
3. To what extent can these findings inform the development of a new parameterisation for initial snow interception?

2 Theory

2.1 Canopy snow mass balance

The change in canopy snow load over time, $\frac{dL}{dt}$ (mm s⁻¹), can be estimated from the mass balance:

$$\frac{dL}{dt} = [q_{sf} - q_{tf} + q_{ros}] - q_{unld} - q_{drip} - q_{wind}^{veg} - q_{sub}^{veg} \quad (1)$$

100 where q_{sf} is the snowfall rate (mm s^{-1}), q_{tf} (mm s^{-1}) is the throughfall rate (mm s^{-1}), q_{ros} (mm s^{-1}) is the rate of rainfall falling on snow intercepted in the canopy, q_{unld} is the canopy snow unloading rate (mm s^{-1}), q_{drip} is the canopy snow drip rate due to canopy snowmelt (mm s^{-1}), q_{wind}^{veg} is the wind transport rate in or out of the control volume (mm s^{-1}), and q_{sub}^{veg} is the 105 intercepted snow sublimation rate (mm s^{-1}). Figure 1 in Cebulski & Pomeroy (2025) presents a visual representation of this mass balance.

106 Interception efficiency, $\frac{I}{P}$ (-), which is the fraction of snowfall intercepted over Δt before
107 ablation, can be calculated as:

$$\frac{I}{P} = \frac{\Delta L}{q_{sf}\Delta t} \quad (2)$$

108 During periods with low air temperatures and low wind speeds, q_{ros} , q_{unld} , q_{drip} , q_{wind}^{veg} , and
109 q_{sub}^{veg} can be assumed negligible and thus the right side of Equation 1 can be simplified and
110 used as an approximation of ΔL to calculate $\frac{I}{P}$ as:

$$\frac{I}{P} = \frac{(q_{sf} - q_{tf})\Delta t}{q_{sf}\Delta t} \quad (3)$$

111 2.2 Hydrometeor trajectory angle

112 Herwitz & Slye (1995) calculate the trajectory angle of a hydrometeor, θ_h , as the departure in
113 degrees ($^\circ$) from a vertical plane as:

$$\theta_h = \arctan \left(\frac{x_h(u_z)}{v_h(D_h)} \right) * \frac{180}{\pi} \quad (4)$$

114 where $v_h(D_h)$ is the terminal fall velocity of the hydrometeor (m s^{-1}), which is a function of
115 the hydrometeor diameter, D_h and $x_h(u_z)$ is the horizontal velocity of the hydrometeor (m
116 s^{-1}) which is a function of the within canopy wind speed, u_z at height above ground, z . In the
117 absence of hydrometeor velocity observations, $v_h(D_h)$ may be approximated from values in the
118 literature (e.g., 0.8 m s^{-1} in Isyumov, 1971) and $x_h(u_z)$ can be approximated by the horizontal
119 wind speed. This assumes the hydrometeors are following fluid points in the atmosphere.

120 **2.3 Within-canopy wind flow**

121 Cionco (1965) showed that, u_z may be approximated using the exponential formula:

$$u_z = u \cdot \exp \left[a \cdot \left(\frac{z}{h_c} - 1 \right) \right] \quad (5)$$

122 where u is the horizontal wind speed at the top of the canopy (m s^{-1}), a is an attenuation
123 coefficient, z is the height above ground (m), and h_c is the average height of the canopy
124 elements. Parviaainen & Pomeroy (2000) provided a method to calculate a using observations
125 from two boreal forest jack pine stands, which was applied in this study.

126 **3 Data and methods**

127 **3.1 Study site**

128 This study was conducted at Fortress Mountain Research Basin (FMRB), Alberta, Canada,
129 -115° W , 51° N , a continental headwater basin in the Canadian Rockies (Figure 1). Data from
130 this study was collected between October 2021 and July 2023 within and surrounding two
131 forest plots adjacent to the FMRB Powerline Station (PWL) and Forest Tower Station (FT)
132 at $\sim 2100 \text{ m}$ above sea level as shown in Figure 1. The average annual precipitation at PWL
133 Station from 2013 to 2023 was 1045 mm, with the average peak annual snow water equivalent
134 (SWE) reaching 465 mm, typically in late April. The PWL plot is adjacent to PWL station and

the FT plot surrounds FT station and both include discontinuous stands of 70% subalpine fir (*Abies lasiocarpa*) and 30% Engelmann spruce (*Picea engelmannii*) (Langs et al., 2020). The canopy closures are 0.51 and 0.29 and the winter leaf area indices are 2.07 and 1.66 for PWL and FT respectively. The average height of the canopy within the PWL plot is 10.5 m and within the FT plot is 7.1 m. In August of 1936, most vegetation in FMRB burned during a large forest fire that affected most of the Kananaskis Valley (Fryer et al., 1988). Following the fire, the forest within the PWL and FT forest plots has naturally regenerated, though some trees have been removed for a powerline clearing and creation of a snow study plot.

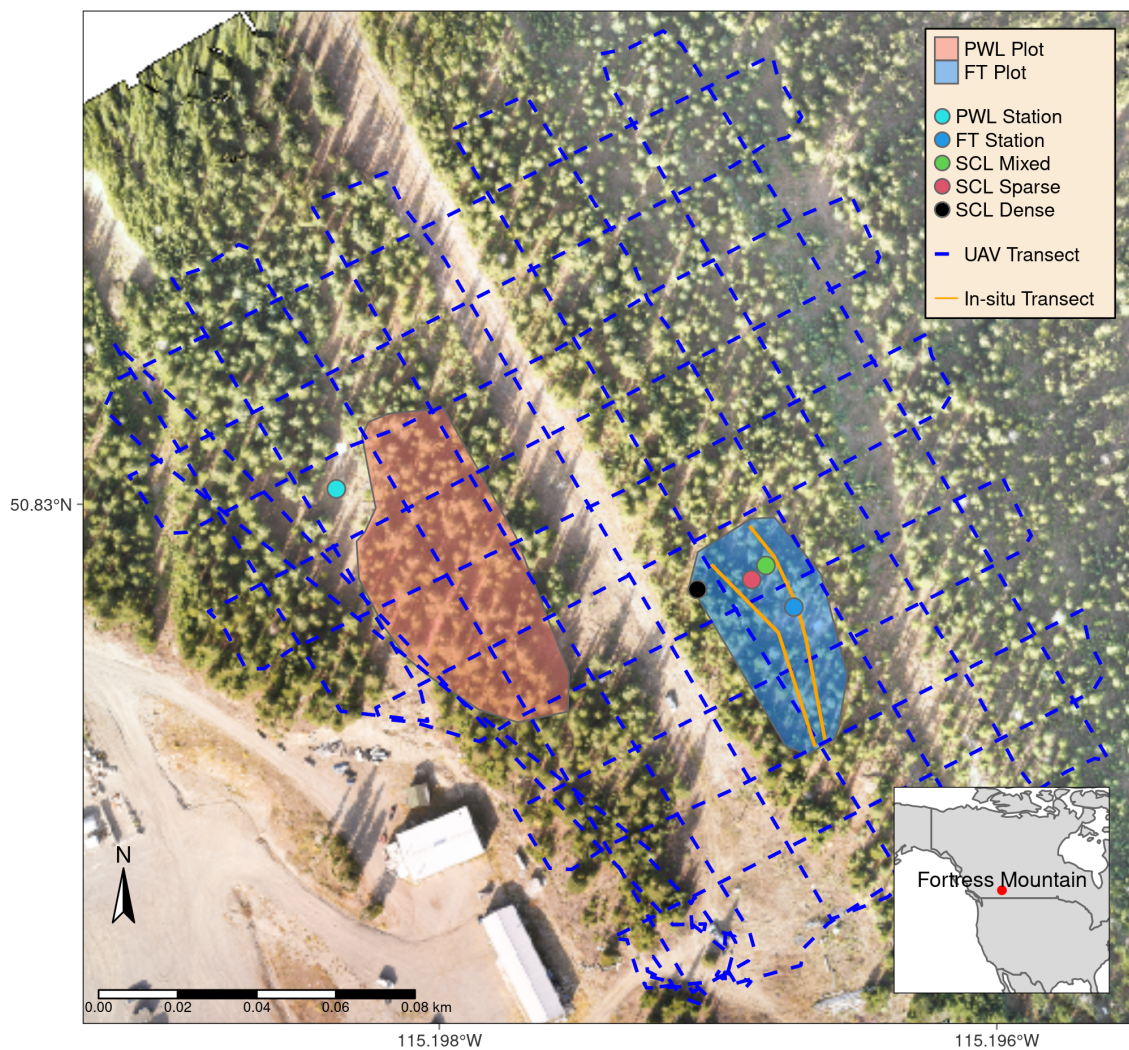


Figure 1: Map showing the location of forest plots, flux towers, subcanopy lysimeter instruments, and survey transects. The inset map on the lower right shows the regional location of Fortress Mountain Research basin.

¹⁴³ **3.2 Meteorological measurements**

¹⁴⁴ Measurements of air temperature and relative humidity (Vaisala model HMP155A), wind speed
¹⁴⁵ and direction (RM Young model 86000 2-D ultrasonic anemometer) were made 4.3 m above
¹⁴⁶ the ground at FT station (Figure 1). Wind speed measurements from a 3-cup anemometer
¹⁴⁷ (Met One model 014A), installed adjacent to the 2-D ultrasonic anemometer at 4.3 m, were
¹⁴⁸ used to fill data gaps in the 2-D ultrasonic anemometer records.

¹⁴⁹ At PWL station, the snowfall rate was measured by an Alter-shielded OTT Pluvio weighing
¹⁵⁰ precipitation gauge 2.6 m above ground, corrected for undercatch following phase correction
¹⁵¹ by Harder & Pomeroy (2013) using the catch efficiency equation of Smith (2007). The in-
¹⁵² strument accuracy of the OTT Pluvio specified in the instrument manual is +/- 0.1 mm or
¹⁵³ 0.2% (whichever is larger). Wind speed for undercatch correction was measured by a 3-cup
¹⁵⁴ anemometer (Met One model 014A) at a height of 2.6 m at PWL station. An optical disdrome-
¹⁵⁵ ter (OTT Parsivel2) provided measurements of hydrometeor particle size and vertical velocity.
¹⁵⁶ All measurements were recorded at 15-min intervals using Campbell Scientific dataloggers,
¹⁵⁷ except the Parsivel2 which was recorded at 1-minute intervals by an onsite computer.

¹⁵⁸ **3.3 Lysimeter measurements**

¹⁵⁹ Three subcanopy lysimeters were installed surrounding the FT Station (Figure 1) to provide
¹⁶⁰ measurements of throughfall for 26 distinct snowfall events, where canopy snow ablation rates
¹⁶¹ were deemed negligible. The subcanopy lysimeter instrument design was adapted from Mac-
¹⁶² Donald (2010) and consisted of a plastic horse-watering trough with an opening of 0.9 m² and
¹⁶³ depth of 20 cm suspended from a load cell (Intertechnology 9363-D3-75-20T1) attached to
¹⁶⁴ an aluminum pipe connected between two trees (Figure 2). The manufacturer-specified com-
¹⁶⁵ bined error of full-scale output for the load cells is +/- 0.02% with a temperature sensitivity
¹⁶⁶ of +/- 0.001%/5°C. The throughfall rate was calculated by dividing the weight of snow in the
¹⁶⁷ subcanopy lysimeter by the cross-sectional area of the opening and determining the rate of
¹⁶⁸ change at hourly intervals. Canopy snow load was estimated using Equation 1, incorporating

169 cumulative throughfall measurements from the subcanopy lysimeters and cumulative snowfall
170 measurements from the PWL gauge for each of the 26 events. Interception efficiency was
171 calculated using Equation 3 and accumulated measurements of snowfall and throughfall at
172 both hourly intervals and within bins of air temperature, wind speed, and initial canopy snow
173 load measured from the weighed tree. The hourly interval measurements resulted in lower
174 accumulations of snowfall and throughfall within each interval and thus had higher relative
175 error compared to the binned measurements. To evaluate the association of hourly intercep-
176 tion efficiency with air temperature, wind speed, and initial canopy snow load, linear models
177 were fitted using ordinary least squares regression. The non-parametric Wilcoxon signed-rank
178 test was also applied to compare the distribution of hourly interception efficiency measure-
179 ments across differing groups of air temperature, wind speed, and initial canopy snow load.
180 Timelapse imagery, mass change on a weighed tree lysimeter (Pomeroy & Schmidt, 1993), and
181 in-situ observations were used to ensure unloading, melt, and wind redistribution of canopy
182 snow was minimal over each interval. Additionally, the throughfall measurements were fil-
183 tered to include observations that coincided with a snowfall rate $> 0 \text{ mm hr}^{-1}$ and a snowfall
184 rate that exceeded the subcanopy lysimeter measured throughfall rate. While these careful
185 manual mitigation and automated filtering strategies substantially reduced the contribution of
186 unloading in the subcanopy lysimeter throughfall measurements, a small contribution is still
187 possible.

188 The subcanopy lysimeters were installed to limit preferential throughfall and unloading by
189 choosing locations with relatively uniform distribution of canopy elements and away from large
190 branches which could preferentially unload snow. The canopy surrounding the subcanopy
191 lysimeters led to reduced wind speeds and reduced the potential for gauge undercatch by
192 these instruments. Photographs of the three subcanopy lysimeters and surrounding canopy
193 are shown in Figure 2. Canopy density measurements, including leaf area index and canopy
194 closure, are summarized in Table 1. A viewing angle from zenith to 60° was selected to
195 describe the surrounding canopy, as a range in hydrometeor trajectory angles was expected
196 to influence the measurements at these locations. The canopy density metrics were measured

197 using hemispherical photography (Nikon Coolpix 4500 and EC-F8 hemispherical lens) for a
198 snow free canopy and analyzed with the hemispheR R package Chianucci & Macek (2023).

199 The weighed tree lysimeter, a live subalpine fir (*Abies lasiocarpa*) tree suspended from a
200 load cell (Artech S-Type 20210-100) measured the weight of canopy snow load (kg). This
201 weight was scaled to an areal estimate of canopy snow load (L , mm) using measurements
202 of areal throughfall (mm) from in-situ snow surveys and snowfall from the PWL Station
203 snowfall gauge, following the method described in Pomeroy & Schmidt (1993). Three sets
204 of in-situ snow survey locations were selected for scaling, each with a mean canopy closure
205 corresponding to one of the subcanopy lysimeters. This resulted in three datasets of canopy
206 snow load from the weighed tree, each reflecting the canopy density of a respective subcanopy
207 lysimeter. Variations in the weighed tree mass were attributed to intercepted snowfall, canopy
208 snow sublimation, unloading, and melt. Since the subcanopy lysimeter estimates of canopy
209 snow load are not influenced by sublimation, they provided a measurement of interception
210 efficiency with less uncertainty and thus were used for the interception efficiency analyses.

Table 1: Leaf area index (LAI) and canopy closure of the three subcanopy lysimeters located proximal to the FT Station.

Name	LAI (-)	Canopy Closure (-)
Sparse	1.56	0.64
Mixed	2.10	0.75
Closed	2.40	0.79

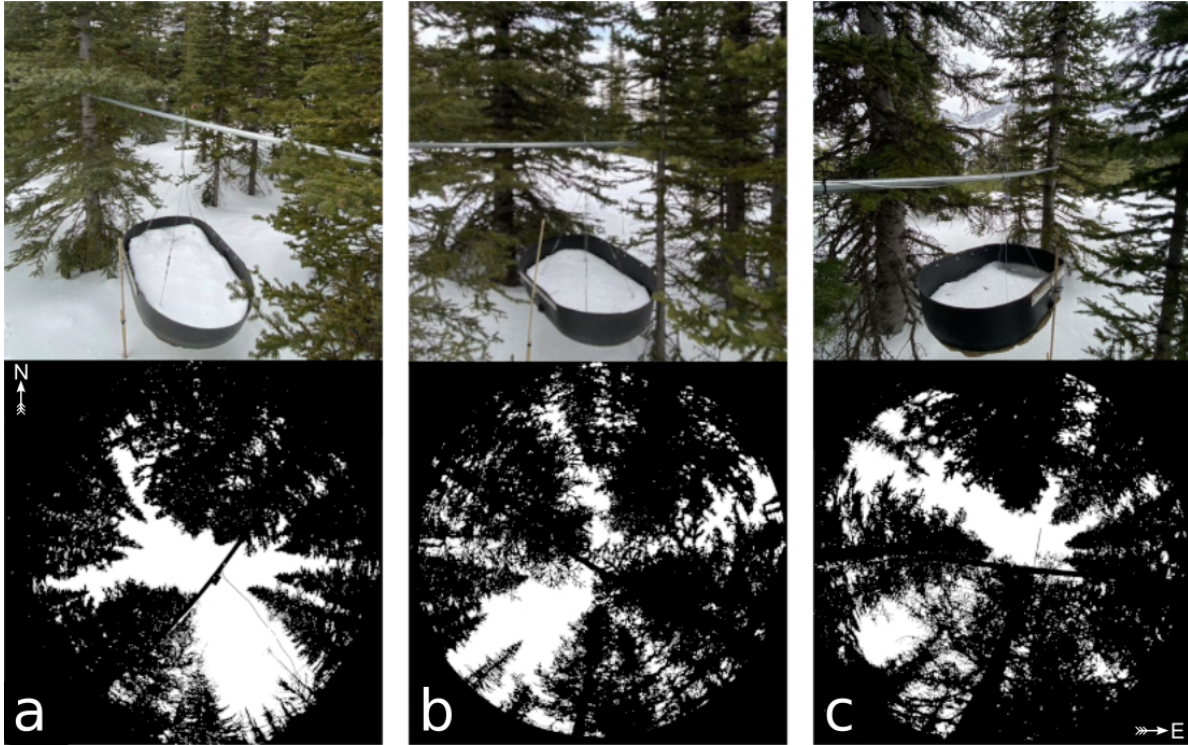


Figure 2: Images of the three subcanopy lysimeter instruments and surrounding canopy located in sparse (a), mixed (b), and dense (c) canopy. The top row presents a side view of each instrument and the bottom row shows hemispherical photographs. These hemispherical images are oriented with north at the top and have been mirrored to provide a view from above (e.g., east is on the right side of each image). See Table 1 for the corresponding canopy density measurement.

3.4 UAV-Lidar data collection and processing

The UAV (FreeFly Alta X) payload included a REIGL miniVUX-2 airborne laser scanner, an Applanix APX-20 inertial measurement unit (IMU) and global navigation satellite system (GNSS). The UAV was flown 90 m above the ground at a speed of 3 m s^{-1} following the path shown in Figure 1. The methods outlined by Harder et al. (2020) and Staines & Pomeroy (2023) were incorporated to reconcile survey lidar, IMU, and GNSS data. A systematic vertical bias of up to 6 cm between UAV-lidar flight lines was observed in the resulting point clouds on March 13th and 14th, 2024 and was attributed to IMU position drift. After strip alignment,

the mean elevation bias in the point clouds compared to the GNSS data was 0.000 m and the RMS error declined from 0.055 m to 0.038 m on March 13th and from 0.033 m to 0.029 m on March 14th. The point cloud density ranged from ~1200 returns m² in sparse forest to ~2200 returns m² in open clearings. Quality control, ground classification, calculation of surface elevation change was conducted on the point cloud data and then converted to 0.05 m resolution rasters. Further quality control was conducted on the 0.05 m raster data to remove values that exceeded the .999th quantile and then resampled to 0.25 m grid cell resolution by taking the median. A detailed description of the UAV, payload, flight settings, and software packages used is provided in the Supporting Information.

3.5 Snow surveys

3.5.1 In-situ snow depth and density

Event-based snow surveys provided measurements of subcanopy throughfall depth and density at 30 locations following the transects shown in Figure 1. These measurements were used to upscale the weighed tree from weight to weight per unit area, assess the accuracy of lidar derived snow depth measurements, and provide a fresh snow density for the calculation of SWE (mm) from the snow depth measurements. Minimal ablation and redistribution of both the surface snowpack and/or snow intercepted in the canopy was crucial to ensure the snow survey measurements were attributed to throughfall. Therefore, only snowfall events with minimal canopy snow ablation as determined through in-situ observations, analysis of timelapse imagery, and mass change on the weighed tree lysimeter were selected. A 1000 cm³ Perla snow density wedge sampler (RIP Cutter, <https://snowmetrics.com/shop/rip-1-cutter-1000-cc/>) was used to measure the density of the fresh snow layer, $\overline{\rho_{tf}}$ (kg m⁻³) from snow pits. Throughfall depth measurements, ΔHS were converted to SWE using the following equation:

$$\Delta SWE_{tf} = \Delta HS \cdot \overline{\rho_{tf}} \quad (6)$$

²⁴² If a pre-event crust layer was present, the depth of post event fresh snow accumulation above
²⁴³ the crust layer was interpreted as throughfall over the event. In the absence of a defined crust
²⁴⁴ layer, the difference in pre- and post-event snow depth to ground was interpreted as event
²⁴⁵ throughfall. Interception efficiency, used in scaling the weighed tree, was calculated using
²⁴⁶ Equation 3 and the ΔSWE_{tf} and cumulative snowfall measurements.

²⁴⁷ **3.5.2 UAV-Lidar snow depth**

²⁴⁸ Two uncrewed aerial vehicle (UAV) lidar surveys were conducted before and after a 24-hour
²⁴⁹ snowfall event that occurred between March 13–14th, 2023 to facilitate the measurement of
²⁵⁰ snow accumulation and canopy density within the FT and PWL forest plots. This period
²⁵¹ was selected based on two criteria: 1) it provided sufficient cumulative snowfall to result in
²⁵² a low relative error in UAV-lidar measured throughfall, and 2) minimal snow redistribution
²⁵³ and ablation was observed, as confirmed by the subcanopy lysimeters, weighed tree, and time-
²⁵⁴ lapse imagery. The change in surface elevation between the two UAV-lidar point clouds was
²⁵⁵ interpreted as the increase in snow accumulation, ΔHS , over the snowfall event. ΔSWE_{tf}
²⁵⁶ was calculated using Equation 6 together with in-situ measurements of $\overline{\rho_{tf}}$. The measurement
²⁵⁷ error of the UAV-lidar derived ΔHS was assessed using the in-situ snow depth observations
²⁵⁸ which is shown in the Supporting Information. Spatially distributed measurements of $\frac{I}{P}$, were
²⁵⁹ then determined using Equation 3 with ΔSWE_{tf} as the throughfall component and cumulative
²⁶⁰ snowfall to the PWL clearing.

²⁶¹ **3.6 UAV-Lidar canopy metrics**

²⁶² The canopy of the study site was characterized from two UAV-lidar point clouds (March 13th
²⁶³ and March 14th) using the voxel ray sampling (VoxRS) methodology for lidar data analysis,
²⁶⁴ as developed by Staines & Pomeroy (2023). This method was chosen for its ability to provide
²⁶⁵ canopy metrics that are less sensitive to the inherent non-uniform nature of lidar sampling
²⁶⁶ data resulting from beam occlusion in vegetation. Using this method radiation transmittance,

²⁶⁷ τ (-), was measured across the hemisphere at a 1° step, e.g., azimuth angles (0°, 1°, ..., 359°)
²⁶⁸ and zenith angles (0°, 1°, ..., 90°) for each 0.25 m grid cell within the FT and PWL forest
²⁶⁹ plots. The fraction of snow-leaf contact area per unit area of ground proposed by Hedstrom
²⁷⁰ & Pomeroy (1998), and hereafter called leaf contact area (C_p), was then calculated as:

$$C_p(C_c, \theta_h) = 1 - \tau \quad (7)$$

$$C_p(C_c, \theta_h) = \begin{cases} 1 - \tau, & \text{if } \theta_h > 0^\circ \\ 1 - \tau \approx C_c, & \theta_h = 0^\circ \end{cases} \quad (8)$$

²⁷¹ where C_p is a function of the canopy cover (C_c) and hydrometeor trajectory angle (θ_h). C_c is
²⁷² the fraction of canopy area to total ground area when viewed from above, which differs from
²⁷³ canopy closure, an angular-derived metric usually measured from the ground perspective.

²⁷⁴ To determine how C_p was associated with interception efficiency at different azimuth and zenith
²⁷⁵ angles over the March 13–14th snowfall event, the entire hemisphere at each grid location was
²⁷⁶ considered. The relationship between interception efficiency and C_p was found to be linear
²⁷⁷ and thus the Pearson Correlation Coefficient was used. The Pearson Correlation Coefficient
²⁷⁸ was computed between a single raster of interception efficiency and each of the 32,760 rasters
²⁷⁹ of C_p measured on March 13th, representing locations across the hemisphere (azimuth [0°, 1°,
²⁸⁰ ..., 359°], zenith angle [0°, 1°, ..., 90°]) at 0.25 m grid cells spanning the FT and PWL forest
²⁸¹ plots.

²⁸² The pair of azimuth and zenith angles corresponding to the C_p that had the highest correlation
²⁸³ with interception efficiency was selected for further analysis. This involved aggregating the
²⁸⁴ interception efficiency and selected C_p rasters from a 0.25 m resolution to 5 m, followed by
²⁸⁵ fitting an ordinary least squares regression between these two variables. The regression was
²⁸⁶ constrained to pass through the origin based on the theoretical principle that the dependent
²⁸⁷ variable must equal zero when the independent variable is zero. To appropriately account

for this constraint, the R^2 values were adjusted according to Equation 10 presented in Kozak & Kozak (1995). The relationship between leaf contact area and simulated trajectory angle was investigated by fitting non-linear models using a non-linear least squares regression. All statistical analyses were performed using the R ‘stats’ package (R Core Team, 2024).

4 Results

4.1 The influence of meteorology on snow interception

Measurements of canopy snow load derived from the subcanopy lysimeters and weighed tree increased linearly with cumulative event snowfall for 26 snowfall events, without evidence of reaching a maximum (Figure 3). Over these events, air temperature ranged from -24.5°C to 1°C, wind speeds at 4.3 m height ranged from calm to 4.6 m s⁻¹ (Table 2), and wind direction was predominately from the southwest during snowfall (Figure 4). Missing canopy snow load measurements, as shown in Figure 3 for certain events, were caused by wiring damage from animals and heavy snow loads. Some of the variability in interception rates within and between different events may be attributed to small amounts of canopy snow unloading and melt, which could not be fully accounted for through the manual and automated filtering mitigation strategies in both the subcanopy lysimeter and weighed tree measurements.

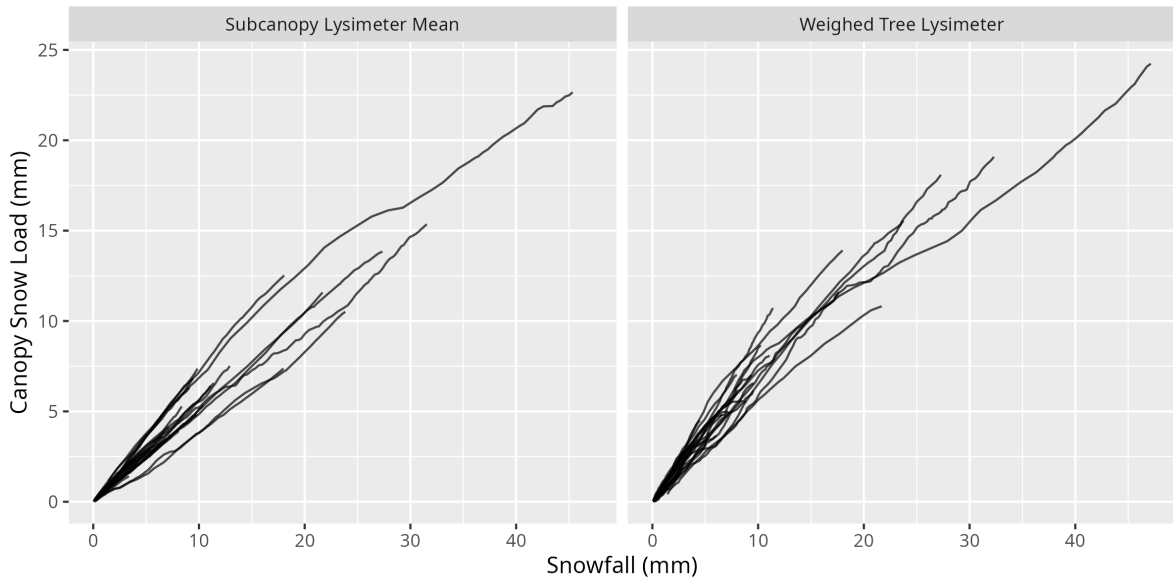


Figure 3: Plot showing the cumulative event snowfall versus canopy snow load calculated using the mean of the three subcanopy lysimeters (left) and weighed tree lysimeter (right) for each of the 26 snowfall events. Both datasets represent canopy snow load for a canopy closure of 0.73 corresponding to the mean of the three subcanopy lysimeter canopies.

Table 2: Meteorology of the 26 snowfall events. Air temperature and wind speed were measured at FT station. Interception efficiency is estimated from cumulative snowfall measured at PWL station and the average cumulative throughfall of all three sub-canopy lysimeters located within the FT forest plot.

Start Date	Air Temperature (°C)			Wind Speed (m/s)			Interception Efficiency (-)			Snowfall (mm)
	Min	Mean	Max	Min	Mean	Max	Min	Mean	Max	
2021-12-23	-6.2	-5.3	-4.6	0.6	3.1	4.6	0.1	0.5	0.9	21.7
2022-01-02	-15.9	-10.8	-5.8	0.2	1.8	4.2	0.0	0.5	1.0	31.6
2022-01-17	-14.8	-7.8	-0.8	0.2	1.1	1.8	0.0	0.6	1.0	12.9
2022-01-31	-24.5	-12.1	-6.4	0.1	1.0	1.7	0.2	0.7	1.0	9.1
2022-02-14	-9.9	-9.0	-8.5	0.4	0.8	1.2	0.2	0.5	0.8	1.7
2022-02-19	-4.7	-3.2	-2.5	1.3	2.3	3.6	0.3	0.6	0.9	11.1
2022-03-01	-8.3	-5.4	-1.0	0.1	1.0	3.1	0.4	0.8	1.0	9.9
2022-03-07	-12.5	-8.6	-4.4	0.3	0.8	1.7	0.3	0.7	1.0	9.5
2022-03-14	-2.7	-2.1	-0.8	1.0	1.6	2.9	0.2	0.6	0.9	8.4
2022-03-19	-3.1	-2.8	-2.5	0.0	0.7	1.3	0.3	0.5	0.6	6.6
2022-03-23	-7.9	-5.3	-0.9	0.8	1.2	1.8	0.4	0.6	0.9	1.6
2022-04-04	-3.5	-2.9	-2.1	0.6	1.0	1.9	0.0	0.4	0.6	3.4
2022-04-18	-5.2	-4.0	-2.7	0.4	1.1	1.9	0.1	0.5	0.9	7.4
2022-04-22	-2.8	-1.8	-0.5	0.4	0.8	1.2	0.1	0.5	1.0	9.8
2022-05-09	-4.9	-4.3	-3.2	0.1	0.4	0.9	0.2	0.5	0.9	8.1
2022-05-19	-4.9	-2.1	0.3	0.1	0.4	0.9	0.2	0.6	0.9	7.1
2022-06-13	-1.1	-0.3	0.6	0.1	0.1	0.4	0.0	0.5	0.9	45.4
2022-12-27	-3.0	-2.7	-1.9	0.6	1.1	1.8	0.2	0.5	0.9	4.5
2023-01-27	-11.5	-7.3	-4.5	0.6	0.9	1.2	0.1	0.5	0.8	10.4
2023-02-19	-14.3	-9.5	-6.3	0.2	0.8	1.4	0.2	0.7	1.0	18.1
2023-02-26	-9.2	-8.4	-6.6	0.2	1.0	2.1	0.3	0.5	1.0	5.4
2023-03-13	-8.9	-3.6	-0.1	0.3	1.3	2.2	0.0	0.5	1.0	27.4
2023-03-24	-7.9	-5.7	-3.5	0.1	0.5	1.2	0.1	0.4	0.7	23.8
2023-04-01	-8.9	-7.7	-4.7	0.1	0.6	1.4	0.4	0.6	0.8	11.4
2023-04-10	-1.1	-0.5	0.3	0.1	0.3	1.0	0.2	0.4	0.6	18.0
2023-05-08	0.2	0.6	1.0	0.4	0.6	0.8	0.6	0.6	0.7	3.5

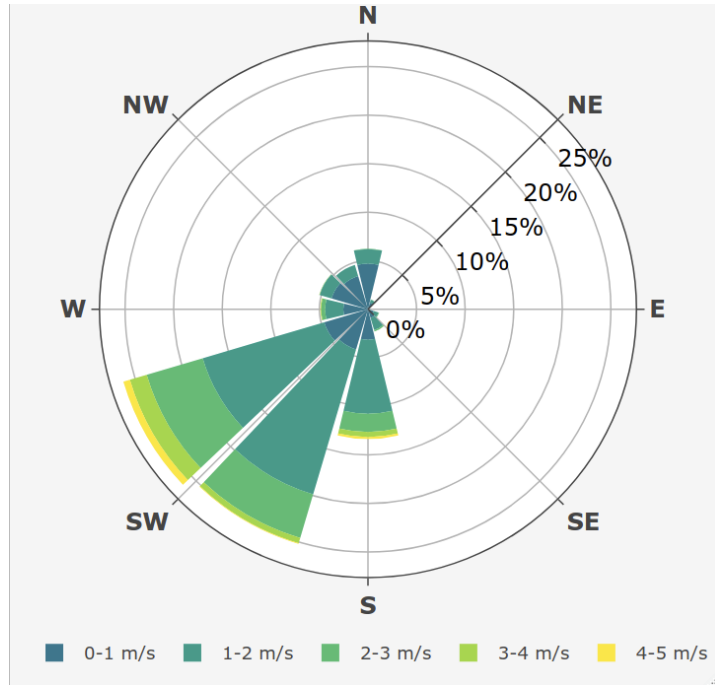


Figure 4: Wind rose showing the frequency of wind speed and direction over the 26 snowfall periods for the ultrasonic anemometer 4.3 m above ground at FT station.

Linear regression analysis revealed no relationship between hourly interception efficiency (from the subcanopy lysimeters) and air temperature, wind speed or canopy snow load, either due to non-significant relationships ($p < 0.05$) and/or weak predictive power ($R^2 < 0.05$) (Table 3). The Wilcoxon test indicated that the difference in hourly interception efficiencies for air temperatures above and below -5°C was not significant ($p > 0.05$, Table 4). Additionally, the interception efficiency across differing bins of air temperature did not show any systematic pattern (Figure 5). Although Figure 5 indicates potentially higher interception efficiency in sparse and mixed canopies at air temperatures below -10°C , these measurements have substantial uncertainty due to heightened instrument error associated with the small accumulations of snowfall and throughfall within these temperature ranges.

When examining wind speed effects, hourly interception efficiencies were found to be significantly higher ($p < 0.05$, Table 4) during periods when wind speeds exceeded 1 m s^{-1} compared

316 to calmer conditions in the sparse and closed canopies using the Wilcoxon test. The binned
317 data also show an increase in interception efficiency with increasing wind speed for these two
318 canopy types (Figure 5). In contrast, the mixed canopy, which had a canopy opening towards
319 the prevailing wind direction (Figure 2), exhibited no significant difference ($p > 0.05$, Table 4).
320 Binned measurements of interception efficiencies corresponding to wind speed bins above 2 m
321 s^{-1} (Figure 5) contained considerable uncertainty resulting from lower snowfall and throughfall
322 accumulation, reducing confidence in these particular findings across all three canopy environ-
323 ments.

324 Significantly higher hourly interception efficiencies ($p < 0.05$, Table 4) were found for initial
325 canopy snow loads below 10 mm compared to heavier snow loads across all three canopy types
326 using the Wilcoxon test. Additionally, the sparse and mixed canopies exhibited significantly
327 lower interception efficiencies ($p < 0.05$) for snow loads below 5 mm compared to those between
328 5–10 mm. The closed canopy displayed a similar initial increase for the binned data visible in
329 Figure 5, but this was not statistically significant for the hourly data ($p > 0.05$, Table 4). For
330 the sparse and closed canopies, a slight increase in binned interception efficiency was observed
331 as snow load increased up to 10 mm, followed by a decline when snow loads exceeded 10 mm
332 (Figure 5). For snow loads exceeding 15 mm, interception efficiency decreased in the sparse
333 and closed canopies, while the mixed canopy showed an increase; however, these measurements
334 carried high uncertainties due to lower accumulated snowfall and throughfall in these higher
335 snow load bins. The differences between the relationships observed in the hourly-interval
336 and binned interception efficiency measurements can be attributed to two factors: greater
337 instrument uncertainty in the hourly measurements and the potential for the dependent and
338 independent variables to be non-stationary over the hourly interval.

Table 3: Statistics corresponding to the ordinary least squares linear regression test between hourly interval measurements of independent variables: mean air temperature, mean wind speed, and initial canopy snow load and the dependent variable mean interception efficiency. The test was run separately for three levels of canopy coverage (C_c) corresponding to each subcanopy lysimeter (SCL).

Dependent Variable	SCL Name	C_c	Adjusted R^2	p-value	n
Air Temperature (°C)	closed	0.79	0.002	0.239	191
Air Temperature (°C)	mixed	0.75	0.024	0.005	298
Air Temperature (°C)	sparse	0.64	0.003	0.208	190
Initial Canopy Snow Load (mm)	closed	0.79	0.029	0.011	188
Initial Canopy Snow Load (mm)	mixed	0.75	0.010	0.049	294
Initial Canopy Snow Load (mm)	sparse	0.64	0.031	0.009	187
Wind Speed (m/s)	closed	0.79	0.025	0.017	191
Wind Speed (m/s)	mixed	0.75	0.034	0.001	298
Wind Speed (m/s)	sparse	0.64	0.046	0.002	190

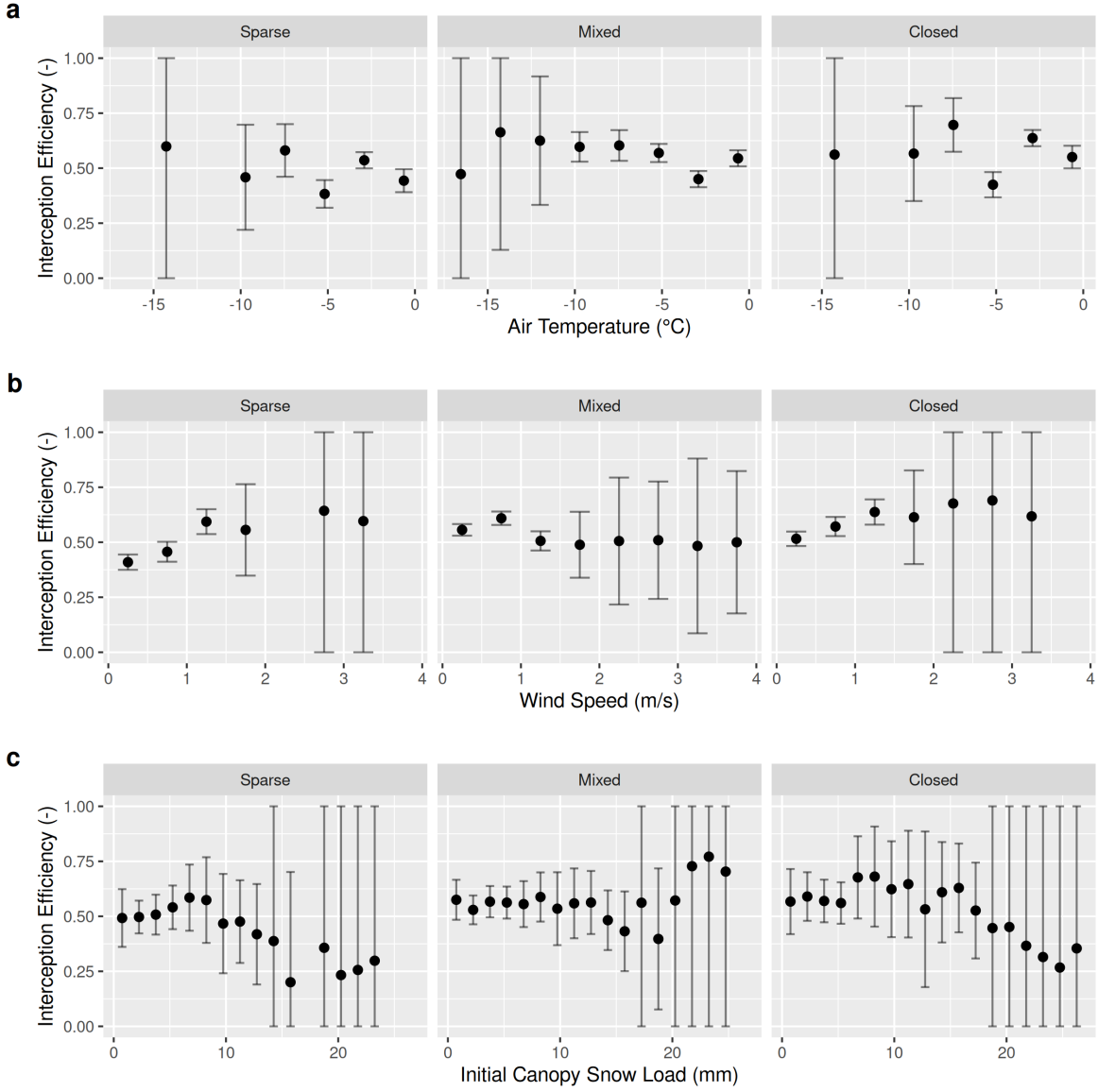


Figure 5: Scatter plots showing the interception efficiency calculated from accumulated snowfall (Pluvio) and throughfall (subcanopy lysimeter) measurements for bins of air temperature, wind speed, and initial canopy snow load (the snow load observed by the weighed tree at the beginning of the timestep) over the 26 snowfall events. The error bars represent the estimated combined instrument error of the snowfall gauge and subcanopy lysimeters.

Table 4: Results of the Wilcoxon signed-rank tests comparing the distributions of hourly interception efficiency (IP) measured by the subcanopy lysimeters for differing groups of air temperatures (Ta), wind speeds (u), and initial canopy snow loads (L). The table reports the canopy corresponding to the subcanopy lysimeter (Canopy), null hypothesis (H_0), p -value, and sample size (n) and median IP for the ‘low’ group (e.g., $Ta < -5^{\circ}\text{C}$) and ‘high’ group (e.g., $Ta = -5^{\circ}\text{C}$).

Canopy	Null Hypothesis (H_0)	p -value	n (low / high)	median I/P	
				(low / high)	Reject H_0
closed	Median IP ($Ta < -5^{\circ}\text{C}$)	0.282	76 / 115	0.56 / 0.62	no
	Median IP ($Ta = -5^{\circ}\text{C}$)				
mixed	Median IP ($Ta < -5^{\circ}\text{C}$)	0.990	165 / 133	0.57 / 0.53	no
	Median IP ($Ta = -5^{\circ}\text{C}$)				
sparse	Median IP ($Ta < -5^{\circ}\text{C}$)	0.864	72 / 118	0.54 / 0.5	no
	Median IP ($Ta = -5^{\circ}\text{C}$)				
closed	Median IP ($u < 1 \text{ m/s}$)	0.004	116 / 75	0.53 / 0.65	yes
	Median IP ($u = 1 \text{ m/s}$)				
mixed	Median IP ($u < 1 \text{ m/s}$)	1.000	165 / 133	0.6 / 0.5	no
	Median IP ($u = 1 \text{ m/s}$)				
sparse	Median IP ($u < 1 \text{ m/s}$)	< 0.001	110 / 80	0.43 / 0.59	yes
	Median IP ($u = 1 \text{ m/s}$)				
closed	Median IP ($L < 10 \text{ mm}$)	0.048	129 / 59	0.62 / 0.57	yes
	Median IP ($L = 10 \text{ mm}$)				
mixed	Median IP ($L < 10 \text{ mm}$)	< 0.001	218 / 76	0.57 / 0.49	yes
	Median IP ($L = 10 \text{ mm}$)				
sparse	Median IP ($L < 10 \text{ mm}$)	< 0.001	157 / 30	0.53 / 0.34	yes
	Median IP ($L = 10 \text{ mm}$)				

Table 4: Results of the Wilcoxon signed-rank tests comparing the distributions of hourly interception efficiency (IP) measured by the subcanopy lysimeters for differing groups of air temperatures (Ta), wind speeds (u), and initial canopy snow loads (L). The table reports the canopy corresponding to the subcanopy lysimeter (Canopy), null hypothesis (H_0), p -value, and sample size (n) and median IP for the ‘low’ group (e.g., Ta < -5°C) and ‘high’ group (e.g., Ta -5°C).

Canopy	Null Hypothesis (H_0)	p -value	median I/P		
			n (low / high)	(low / high)	Reject H_0
closed	Median IP (L < 5 mm)	0.333	62 / 67	0.62 / 0.62	no
	Median IP (5 mm L < 10 mm)				
mixed	Median IP (L < 5 mm)	0.019	117 / 101	0.57 / 0.61	yes
	Median IP (5 mm L < 10 mm)				
sparse	Median IP (L < 5 mm)	0.043	90 / 67	0.49 / 0.6	yes
	Median IP (5 mm L < 10 mm)				

339 4.2 The influence of canopy density on snow interception

340 UAV-lidar measurements of throughfall and canopy density provide insights on how the forest
 341 canopy influenced subcanopy snow accumulation during a wind-driven snowfall event between
 342 March 13–14th. This event totaled 28.7 mm of snowfall at PWL station and was characterized
 343 by a transition from low rates of snowfall and air temperatures near 0°C to higher rates of
 344 snowfall by late afternoon on March 13th coinciding with air temperatures around -2.5 °C. An
 345 average wind speed of 1.3 m s⁻¹ and direction of 188° was observed 4.3 m above the ground
 346 at FT Station. The mean observed hydrometeor terminal fall velocity observed over the event
 347 was 0.9 m s⁻¹.

348 The throughfall depth measured by UAV-lidar aligned with the in-situ manual measurements

resulting in a mean bias of -0.001 m and RMSE of 0.024 m. More details on the accuracy of UAV-lidar snow depth measurements are provided in the Supporting Information section. Figure 6 shows the spatial distribution of throughfall and interception efficiency at the PWL and FT forest plots. Reduced throughfall and greater interception efficiency was observed on the north (lee) side of individual trees, which may be due to non-vertical hydrometeor trajectories caused by the steady southerly winds observed over this event. Transparent areas within the forest plots in Figure 6 represent grid cells that did not have any lidar ground returns (e.g., under dense canopy proximal to tree trunks) or were masked due to disturbance (e.g., walking paths in clearings). Visual observations on March 13th and 14th confirmed non-vertical hydrometeor trajectories and increased canopy snow loads were observed on the windward side of individual trees. This effect is more apparent in the PWL forest plot than the FT forest plot and may be attributed to the taller trees and higher canopy cover of the PWL forest plot compared to the FT forest plot (Figure 6).

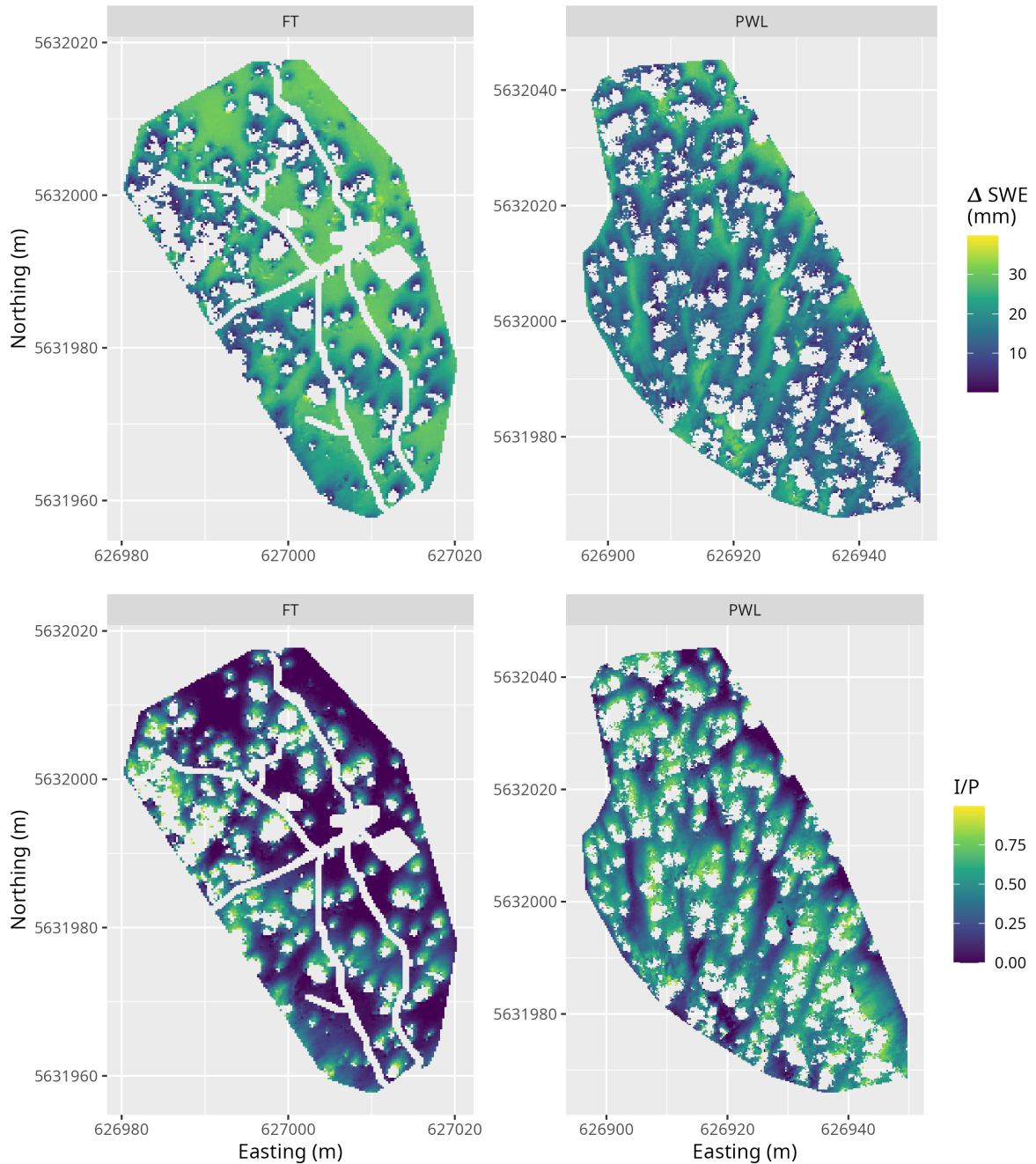


Figure 6: UAV-lidar measurements of the change in snow water equivalent, SWE (mm) and interception efficiency, I/P (-), over the March 13–14th 24-hour snowfall event for the FT and PWL forest plots at a 0.25 m resolution. See the location of the two forest plots in Figure 1.

362 The VoxRS measurements of C_p on March 13th were selected for analysis and represent the
 363 canopy of both forest plots without snow. Little difference in C_p was observed between the
 364 March 13th and March 14th measurements. A strong linear correlation between C_p measured
 365 on March 13th and interception efficiency was observed towards the southern portion of the
 366 hemisphere, aligning with the average event wind direction (Figure 7). For the PWL forest
 367 plot, the upper 97.5th percentile of the Pearson Correlation Coefficient (ρ_p) values were found
 368 between azimuth angles of 167°–217°. Similarly, for the FT forest plot, the upper 97.5th
 369 percentile of ρ_p was found between azimuth angles of 171°–223°. The zenith angle found
 370 to have the highest correlation over this azimuth range was 22° ($\rho_p = 0.7$) and 21° ($\rho_p =$
 371 0.83) for PWL and FT respectively. The high correlation coefficients found for non-vertical
 372 zenith angles for both PWL and FT are hypothesized to result from non-vertical hydrometeor
 373 trajectories.

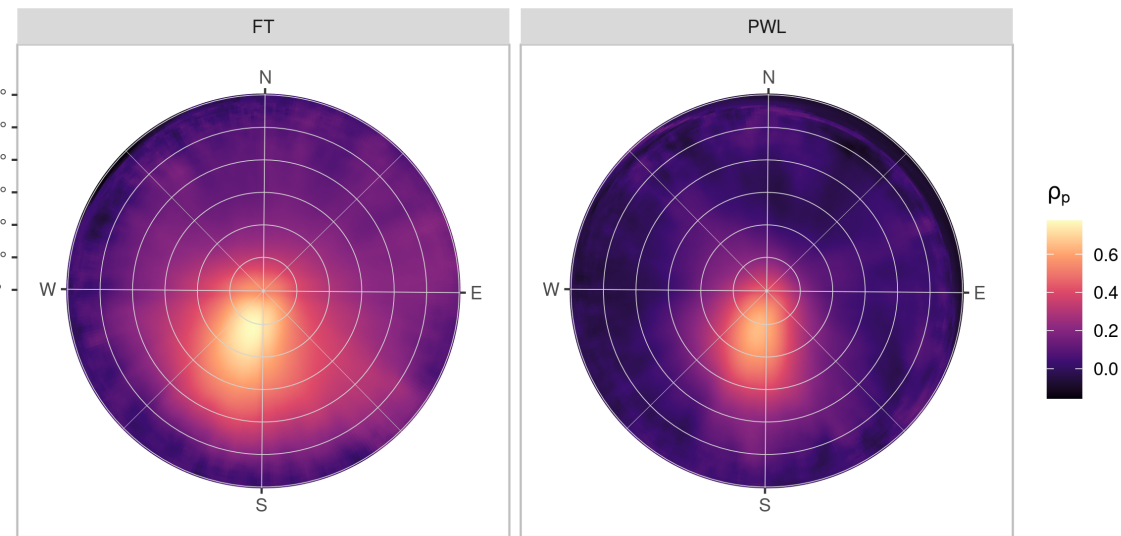


Figure 7: The Pearson Correlation Coefficient between rasters (0.25 m resolution) of interception efficiency and leaf contact area (measured on March 13th) for each grid cell across the study site for each azimuth angles (0°, 1°, ..., 359°) and zenith angles (0°, 1°, ..., 90°) for the FT (left) and PWL (right) forest plots.

374 The spatial distribution of C_p measurements, selected based on the vector corresponding to the

azimuth and zenith angles observed to have the highest correlation with interception efficiency in Figure 7, is shown in Figure 8. These C_p measurements generally align with the spatial distribution of interception efficiency and throughfall (Figure 6).

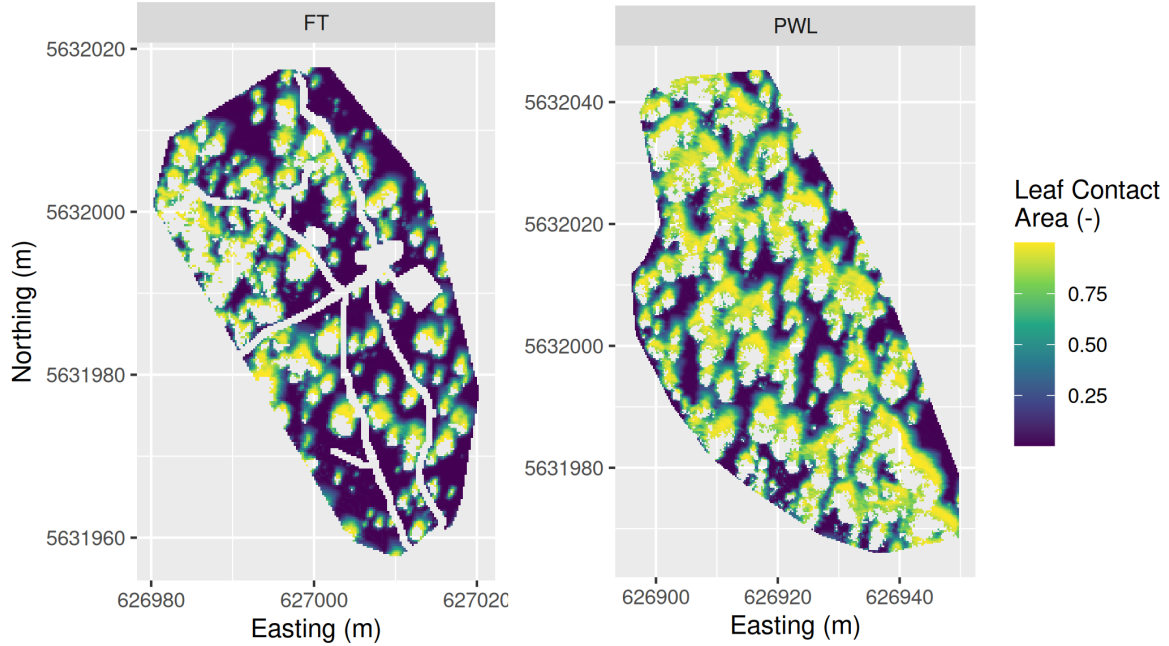


Figure 8: UAV-lidar VoxRS measurements of leaf contact area measured on March 13th for the PWL and FT forest plots for zenith angles (PWL = 22°, FT = 21°) and azimuth angles (PWL = 167°, 178°, ... 217°; FT = 171°, 172°, ... 223°).

The correlation between interception efficiency (Figure 6) and C_p (Figure 8), resampled to a 5 m grid resolution, was higher compared to the association with leaf contact angle measured at a zenith angle of 0° (Figure 9). The stronger association for the vector-based calculation is hypothesized to stem from a more accurate representation of the snowfall contact area and suggests that adjusted C_p is a useful predictor of interception efficiency before ablation. An ordinary least squares linear regression forced through the origin was fit to the observed data

384 points using the following equation:

$$\frac{I}{P} = C_p(C_c, \theta_h) \cdot \alpha \quad (9)$$

385 where α is an efficiency constant which determines the fraction of snowflakes that contact the
 386 C_p elements and are stored in the canopy (i.e., intercepted) before canopy snow unloading or
 387 ablation processes begin.

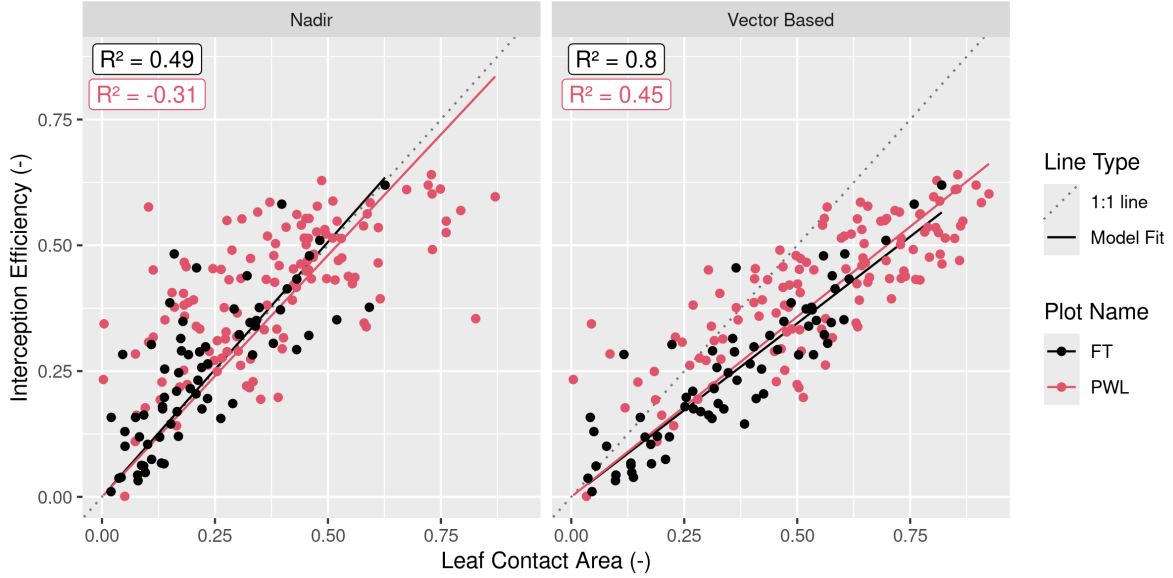


Figure 9: Scatter plots showing the relationship between leaf contact area and interception efficiency rasters resampled to a 5 m grid cell resolution. The left plot (nadir) shows canopy coverage and the right plot (Vector Based) shows the leaf contact area averaged over rasters with zenith angles (PWL = 22°, FT = 21°) and azimuth angles (PWL = 167°, 178°, ... 217°; FT = 171°, 172°, ... 223°). The solid lines (Model fit) show an ordinary least squares linear regression forced through the origin and fitted to the PWL (red) and FT (black) data and the light grey dotted line shows a 1:1 line. The R^2 values for the four different models are shown in the upper left of each panel calculated following the methods outlined in Kozak & Kozak (1995).

388 For the vector-based model, the relationship between interception efficiency and C_p resulted
 389 in R^2 values of 0.45 and 0.8 for PWL and FT respectively. Model error statistics show the

vector-based model provided a better prediction of interception efficiency compared to the nadir canopy coverage measurements (Table 5). The increase in interception efficiency with C_p follows a reduced slope compared to the nadir models with α values of 0.72 and 0.69 for the PWL and FT vector-based models respectively. The reduced slope for the vector-based models may be due to snowflakes that weaved through and/or bounced off branch elements in addition to UAV-lidar throughfall measurement uncertainty which may have been slightly affected by unloading and redistribution. These processes would have reduced the fraction of snowfall that was stored in the canopy. Some of the scatter observed in the nadir model shown in Figure 9 may be explained by grid cells within canopy gaps which observed a greater interception efficiency compared to the corresponding canopy cover. Conversely, grid cells where interception efficiency is less than the canopy cover, may be affected by non-vertical trajectory hydrometeors making their way underneath the canopy as observed by the reduced interception efficiency on the windward edges of individual trees in Figure 6.

Table 5: Summary of error statistics for the linear regression models relating leaf contact area to interception efficiency, presented in Figure 9. The Mean bias is the difference in the model and observed values, MAE is the mean of the absolute error, RMS Error is the root mean squared error, R^2 is the coefficient of determination adjusted using Equation 10 in Kozak & Kozak (1995).

Plot	Canopy	Model	Mean Bias	MAE	RMS	
Name	Calculation	Slope (-)	(-)	(-)	Error (-)	R^2
FT	Nadir	1.01	0.024	0.072	0.101	0.49
FT	Vector Based	0.69	0.003	0.047	0.063	0.80
PWL	Nadir	0.96	0.049	0.115	0.148	-0.31
PWL	Vector Based	0.72	0.020	0.079	0.096	0.45

403 **4.3 The combined influence of trajectory angle and canopy density on snow
404 interception**

405 VoxRS measurements of C_p prior to snowfall on March 13th, increased substantially with
406 simulated hydrometeor trajectory angle and corresponding simulated wind speed (Figure 10).
407 The standard deviation in VoxRS measured C_p , illustrated by the shaded area in Figure 10,
408 exhibits the broad range in values for individual grid cells across each forest plot. Despite
409 this large scatter, a systematic increase in the mean C_p across both forest plots results from a
410 rise in the number of canopy elements for more horizontal angles, when averaged across each
411 forest plot, over all azimuth angles (see top left panel Figure 10). This results in a large rise
412 in C_p over relatively common wind speeds. For example, with a wind speed of 1 m s⁻¹ and
413 estimated trajectory angle of 48°, C_p would increase by 0.31 and 0.28 for the PWL and FT
414 forest plots respectively (Figure 10). The increase in C_p from nadir measured canopy coverage
415 with increasing trajectory angle exhibits a similar relationship for both forest plots FT and
416 PWL until trajectory angles reach approximately 60° (see bottom row of Figure 10). Beyond
417 60°, the PWL rate of increase slows as the C_p approaches 1.0, while the FT plot, which has
418 lower canopy coverage, continues to rise until around 75° as a C_p of 1.0 is approached. C_p was

⁴¹⁹ also quantified across trajectory angles for both PWL and FT on March 14th, post snowfall,
⁴²⁰ and showed a negligible increase in C_p compared to C_p measured on March 13th without snow
⁴²¹ in the canopy.

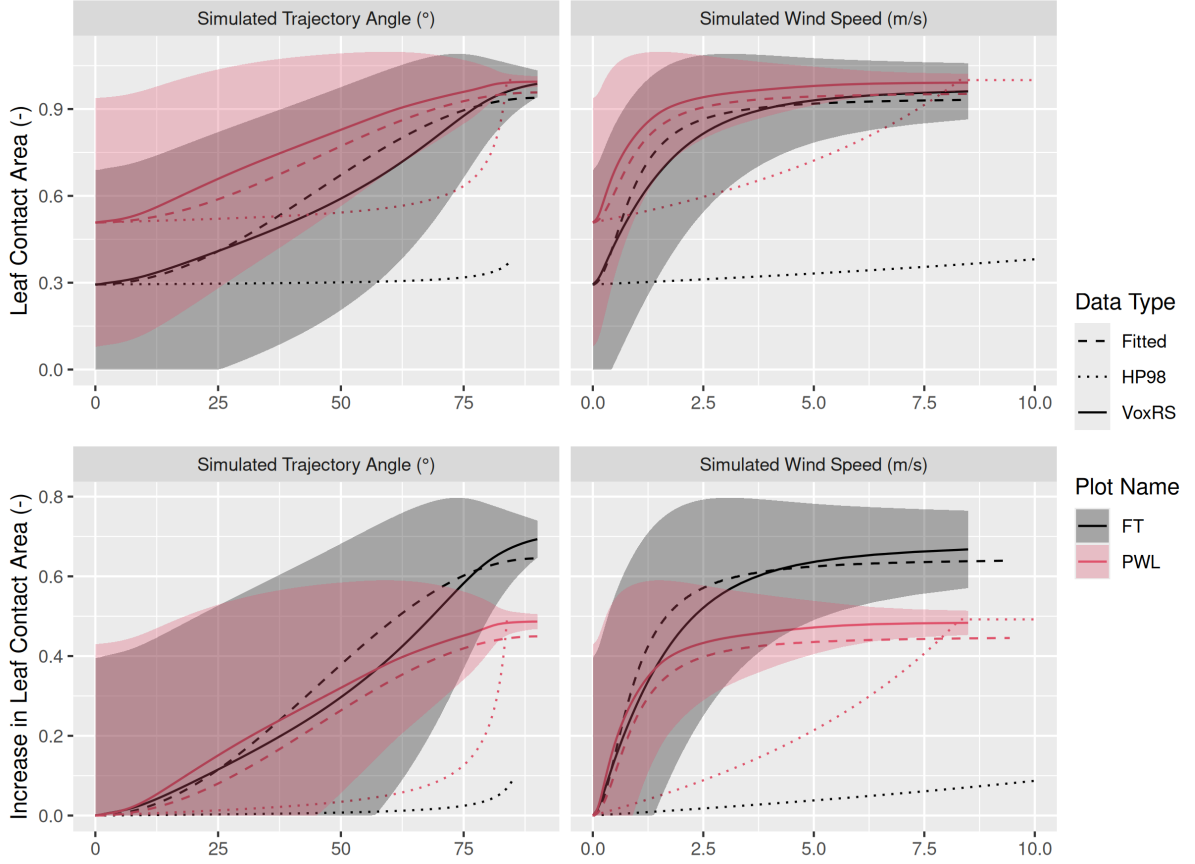


Figure 10: Plots showing the relationship between hydrometeor trajectory angle (left column) and wind speed (right column) with mean plot-wide snow-leaf contact area, C_p (top row) and the increase in mean plot-wide C_p , i.e., $C_p - C_c$ (bottom row). The simulated hydrometeor trajectory angle is measured as degrees from zenith. Simulated wind speed was calculated as a function of hydrometeor trajectory angle by rearranging Equation 4 and an observed event hydrometeor fall velocity of 0.9 m s^{-1} . The solid lines (VoxRS) represent the mean C_p (top row) or increase in mean C_p (bottom row) for a single zenith angle observed from VoxRS across all grid cells for each forest plot and across all azimuth angles. The shaded area represents one standard deviation above and below the observed VoxRS mean. The dashed lines (Fitted) represent predictions from Equation 10 (top row) and Equation 11 (bottom row). The dotted lines (HP98) represent the predictions from Equation 10 in Hedstrom & Pomeroy (1998). A forested downwind distance of 100 m was assumed for the HP98 calculation.

⁴²² A function is proposed here to calculate plot-scale leaf contact area, C_p (-):

$$C_p = C_c + C_{inc}(\theta_h, C_c) \quad (10)$$

423 where C_{inc} represents the increase in leaf contact area from nadir measured canopy coverage
 424 (C_c), and is a function of θ_h and C_c . To estimate C_{inc} in the absence of detailed canopy
 425 measurements, the following function is proposed:

$$C_{inc} = (1 - C_c) \cdot f(\theta_h) \quad (11)$$

426 where $1 - C_c$ quantifies the available void space within the canopy and $f(\theta_h)$ represents the
 427 fraction of that space contributing to increased leaf contact area. Here, $f(\theta_h)$ is approximated
 428 as:

$$f(\theta_h) = b \cdot \sin(\theta_h)^2 \quad (12)$$

429 where b is a fitting coefficient, estimated to be ~ 0.91 through a non-linear least squares re-
 430 gression fit to the VoxRS measurements at both FT and PWL. The term $\sin(\theta_h)^2$ reflects the
 431 relative increase in snow-leaf contact area, which in turn leads to a proportional decrease in
 432 the canopy void space $(1 - C_c)$. Thus, for θ_h of 0° , C_p is equal to the canopy cover. In contrast,
 433 for θ_h close to 90° , C_p approaches a value of 1.0. The assumptions of Equation 12 include
 434 that C_c represents a measurement of continuous canopy cover without large open areas many
 435 times greater than the mean canopy height and that snowfall trajectories are linear.

436 Simulated C_p using Equation 10 is shown in the dashed lines in the top row of Figure 10
 437 and follows the VoxRS-measured mean C_p closely. Model error statistics demonstrate that
 438 Equation 11 performed well, with a mean bias and RMSE of -0.05 (-) and 0.05 (-) for PWL, and
 439 0.03 (-) and 0.05 (-) for FT respectively (Table 6). In contrast, the Hedstrom & Pomeroy (1998)
 440 method produced significantly less accurate estimates of C_p , with a mean bias and RMSE of
 441 -0.2 (-) and 0.23 (-) for PWL, and -0.26 (-) and 0.32 (-) for FT respectively (Table 6).

Table 6: Model error statistics calculated for the prediction of leaf contact area from trajectory angle using Equation 11 and Equation 10 from Hedstrom & Pomeroy (1998) (HP98) for the PWL and FT forest plots. Mean bias is the difference in the model and observed values, MAE is the mean of the absolute error, RMS Error is the root mean squared error and R^2 is the coefficient of determination. The units for all metrics are dimensionless. A forested downwind distance of 100 m was used for the HP98 calculation.

Model	Plot Name	Mean Bias (-)	MAE (-)	RMS Error (-)	R^2
HP98	FT	-0.26	0.26	0.32	-0.97
HP98	PWL	-0.20	0.20	0.23	-0.96
Eq. 10	FT	0.03	0.04	0.05	0.95
Eq. 10	PWL	-0.05	0.05	0.05	0.90

442 4.4 Throughfall model performance

443 The performance of the interception efficiency (Equation 9) and leaf contact area (Equation 10)
 444 parameterisations in estimating event throughfall was assessed against UAV-lidar measure-
 445 ments of throughfall at the plot scale for the March 13–14th snowfall event. In this assessment,
 446 the hydrometeor trajectory angle was approximated using Equation 4 combined with the mean
 447 event wind speed at one-third the mean canopy height (estimated from Equation 5 and the
 448 observed wind speed at FT station) and hydrometeor terminal velocity (measured at PWL
 449 station). Leaf contact area was then estimated using Equation 10 for the PWL and FT plots,
 450 incorporating the approximated hydrometeor trajectory angle and observed canopy cover (C_c)
 451 from the VoxRS dataset. Interception efficiency was calculated using Equation 9 with the
 452 estimated leaf contact area from Equation 10 and accumulated snowfall measured at PWL
 453 station for the event. An α value, used in Equation 9, of 0.978 (-) was found through calibra-
 454 tion which provided the best fit between observed and simulated interception efficiency at the
 455 plot scale for both FT and PWL.

456 The new vector-based parameterisation closely matched the UAV-lidar measurements of

457 throughfall (Figure 11). Modelled throughfall from the vector-based model was 17.2 mm
 458 compared to the measured throughfall of 16.6 mm for PWL. For FT, the vector-based
 459 modelled throughfall was 21.5 mm, while the measured values were 22.1 mm. The
 460 vector-based model shows a lower mean bias of -0.6 mm for PWL and 0.6 mm for FT, in
 461 contrast to the nadir-based model, which overestimated throughfall for both plots (Table 7).
 462 This overestimation arose from the nadir-based model's approximation of leaf contact area
 463 from canopy coverage measurements (without adjustment via Equation 10), which yielded a
 464 reduced estimated contact area and consequently underestimated canopy snow interception.

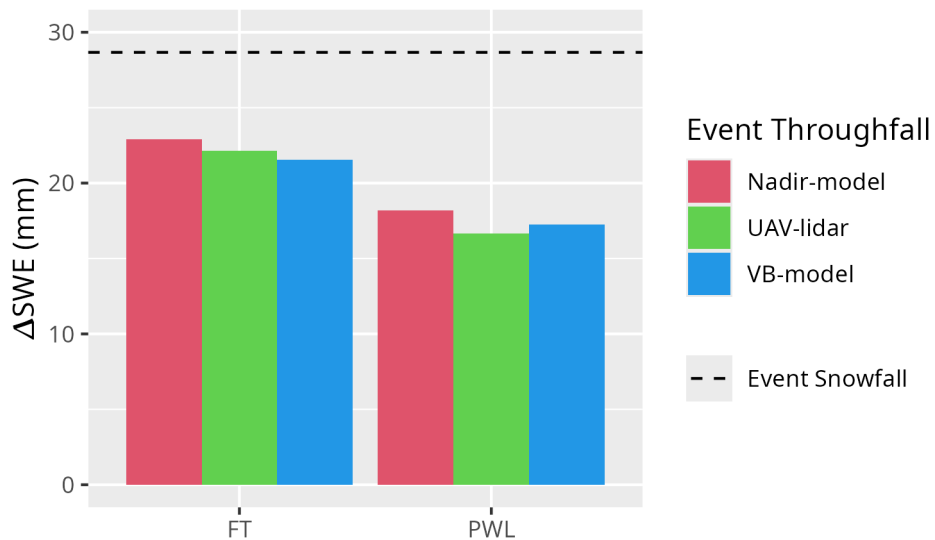


Figure 11: Bar chart comparing the observed and modelled mean change in throughfall (ΔSWE , mm) over the March 13-14th snowfall event averaged over forest plots FT and PWL. The 'Nadir-model' calculated interception efficiency as a function of canopy coverage and the Vector-based 'VB-model' used Equation 9 with C_p adjusted for trajectory angle. 'UAV-lidar' corresponds to throughfall calculated using Equation 6 incorporating UAV-lidar snow depth and snow density from in-situ snow pits. The black horizontal dashed line shows the accumulated SWE (mm) over the snowfall event to the PWL station open clearing.

Table 7: Model error statistics for model estimates of snow interception efficiency (I/P) and throughfall (TF) compared to measurements of I/P and TF using UAV-lidar averaged over the FT and PWL forest plots. Units for I/P are (-) and TF are (mm). The vector-based model utilized Equation 9 with C_p adjusted for trajectory angle. The nadir model also utilized Equation 9 but was not adjusted for trajectory angle and thus C_c was used instead of C_p . The ‘Obs. Value’ column contains measurements from UAV-lidar while the ‘Mod. Value’ column contains the modelled values. The mean bias was calculated as observed minus modelled and percent error is the percent error between predicted and observed values.

Plot	Model	Value		Obs.	Mod.	Mean	Perc.
Plot	Type	Name	Units	Value	Value	Bias	Error
FT	VB-model	I/P	-	0.23	0.25	-0.02	-9.01
FT	Nadir-model	I/P	-	0.23	0.20	0.03	12.10
FT	VB-model	TF	mm	22.12	21.53	0.59	2.67
FT	Nadir-model	TF	mm	22.12	22.91	-0.79	-3.58
PWL	VB-model	I/P	-	0.42	0.40	0.02	4.91
PWL	Nadir-model	I/P	-	0.42	0.37	0.05	12.95
PWL	VB-model	TF	mm	16.64	17.24	-0.59	-3.55
PWL	Nadir-model	TF	mm	16.64	18.20	-1.56	-9.35

465 **5 Discussion**

466 The point scale observations presented in Figure 5 indicate that air temperature had little in-
467 fluence on initial interception efficiency during periods where melt and unloading of snow were
468 less likely. This finding aligns with Storck et al. (2002), who observed that variations in air
469 temperature did not significantly affect initial interception efficiency. While other studies have
470 reported both positive (Andreadis et al., 2009; Katsushima et al., 2023; Roth & Nolin, 2019)
471 and negative (Hedstrom & Pomeroy, 1998; Schmidt & Gluns, 1991) relationships between air
472 temperature and snow interception, the limited association observed here may be explained by
473 competing temperature-dependent processes. Warmer temperatures simultaneously increase
474 branch flexibility, reducing C_p (Schmidt & Gluns, 1991; Schmidt & Pomeroy, 1990) and en-
475 hance snow cohesion and adhesion, increasing interception efficiency (Katsushima et al., 2023;
476 Kobayashi, 1987; Pfister & Schneebeli, 1999).

477 Initial interception efficiency was found to increase with wind speed at two locations which
478 were sheltered from the predominant wind direction (Figure 5). This is hypothesized to be due
479 to an increase in C_p associated with non-vertical hydrometeor trajectories, as demonstrated
480 by observations during a wind-driven snowfall event (Figure 6) and analysis of canopy density
481 data (Figure 10). These findings are also consistent with observations by Schmidt & Troendle
482 (1989) who observed a slight increase in snowfall interception with increasing wind speeds
483 up to 6 m s^{-1} , Staines & Pomeroy (2023) who observed reduced canopy transmittance with
484 increasing angle from zenith, and studies of rainfall interception by Herwitz & Slye (1995) and
485 Van Stan et al. (2011).

486 The slight increase in interception efficiency for smaller canopy snow loads and decline for larger
487 canopy snow loads is attributed to the influence of canopy snow load on C_p (Figure 5). Whilst
488 small, this effect is consistent with the theory proposed by Satterlund & Haupt (1967) that
489 interception efficiency increases as the canopy fills with snow bridging gaps in the canopy, while
490 later declining due to branch bending and decreased canopy cover. However, at the plot-scale,
491 Staines & Pomeroy (2023) showed that these two processes may partially compensate for each

other as C_p increases for closed canopies, as new snow bridges form in the canopy, but decreases in partially open canopy due to branch bending (i.e., Fig. 2 in Schmidt & Gluns, 1991). Still, the increase in C_p resulting from snow load in Staines & Pomeroy (2023) was small compared to the substantial rise in C_p due to trajectory angle presented in their study; which corroborates with the plot-scale observations of C_p in this study (Figure 10). Additional observations by Watanabe & Ozeki (1964), Calder (1990), and Storck et al. (2002) support the findings in Figure 3 showing a linear increase in canopy snow load with increasing snowfall. Further evidence in support of the relatively small influence of canopy snow load on C_p , is provided by Lundquist et al. (2021) who reported improved simulation of subcanopy snow accumulation without the use of a maximum canopy snow load, when linked with a comprehensive canopy snow ablation routine. The low sensitivity to canopy snow load found here may result from reduced inclusion of ablation processes in our measurements, limited influence of snow load on C_p at this site, and/or the compensatory effects described by Satterlund & Haupt (1967).

The limited influence of air temperature and canopy snow load on initial interception reported here differs from the theories underpinning existing snow interception parameterisations (Andreadis et al., 2009; Hedstrom & Pomeroy, 1998; Moeser et al., 2015b; Satterlund & Haupt, 1967). Cebulski & Pomeroy (2025) note studies that have identified a relationship between air temperature and/or snow load and interception efficiency (Katsushima et al., 2023; Roth & Nolin, 2019; Schmidt & Gluns, 1991) did not specifically examine initial interception prior to canopy snow ablation. In addition, since a maximum canopy snow load was not observed in this study, the air temperature dependent canopy snow load capacities included in the Hedstrom & Pomeroy (1998) and Andreadis et al. (2009) models were not applicable. Since canopy snow ablation is strongly correlated with air temperature and snow load (Ellis et al., 2010; Floyd, 2012; Hedstrom & Pomeroy, 1998; Roesch et al., 2001) some of the previously observed relationships related to these variables may be explained by changes in ablation rather than initial interception. The coupling of ablation processes within existing models may contribute to overestimates of throughfall and canopy snow unloading when combined with other canopy snow ablation parameterisations due to ‘double counting’ (Cebulski & Pomeroy, 2025).

To address these issues, a new vector-based snow interception parameterisation is presented (Equation 9) which calculates initial interception efficiency as a function of C_p and an efficiency constant, α . This new parameterisation allows for canopy snow loading processes to be isolated from canopy snow ablation processes and is consistent with current rainfall interception theory (Valante et al., 1997; Zhong et al., 2022). Equation 9 differs only slightly from the original Hedstrom & Pomeroy (1998) parameterisation (see Equation 6 in Hedstrom & Pomeroy 1998), in that it does not calculate interception efficiency as a function of canopy snow load and from the Storck et al. (2002) parameterisation who found interception efficiency to be constant. Further research is needed to explore how processes such as the increased cohesion and adhesion of snowfall to the canopy at warm temperatures, as observed by Kobayashi (1987), Pfister & Schneebeli (1999), as well as hydrometeor velocity, particle size, and shape suggested by (Katsushima et al., 2023), may influence the α parameter, although these effects were not observed in this study. Since Equation 9 intentionally excludes processes attributed to canopy snow ablation that were previously included in earlier snow interception models, these ablation processes must be incorporated in canopy snow ablation parameterisations to fully represent the canopy snow mass balance.

The exponential relationship proposed by Hedstrom & Pomeroy (1998) to scale C_p with wind speed failed to reproduce the observations presented in Figure 10. Instead, plot-wide C_p was found to increase as function of hydrometeor trajectory angle and canopy cover. However, the large scatter in C_p measurements shown in Figure 10 suggests Equation 11 is only applicable at the forest stand scale, or larger, where the sub-metre variability in C_p resulting from directional differences averages out. Canopy cover measurements at larger scales may lack sufficient resolution to identify large open area components of forests, where the assumptions of Equation 10 would not be valid, and C_p should be estimated using horizontal canopy cover without adjusting for snowfall trajectory angle. If fine-scale canopy observations are available, canopy structure metrics such as the gap area indices described in Moeser et al. (2015a) could be helpful for identifying large gaps in the canopy. Moreover, our measurements show the hydrometeor trajectory angle required for Equation 11, can be approximated from Equation 4

incorporating the hydrometeor fall velocity and the mean horizontal wind speed selected at one-third of the canopy height. This is consistent with Katsushima et al. (2023), who also proposed using a wind speed at one-third the canopy height for modelling unloading of canopy snow. The transferability of the snow-leaf contact area equation (Equation 11) remains uncertain, as it has only been tested at a single site with two tree species, and the relationship of C_p with environmental factors is expected to vary across different climate conditions, canopy structures, densities, species, and ages. Additionally, Equation 4 assumes a linear hydrometeor trajectory, and does not consider non-linear patterns such as wind flow directions around tree elements, turbulent flow, or differences in wind speed with height. Staines & Pomeroy (2023) showed, at a proximal montane spruce-fir forest, that backflows and large eddies that occur within the canopy can contribute to mixed responses. Therefore, further testing and modification of Equation 11 is needed in diverse forest environments.

Although the vector-based model showed relatively modest improvement over the nadir model, it is preferred due to its lower error compared to the UAV-lidar measurements and better representation of physical processes. Developed and tested at the forest plot scale (hectares), the vector-based model is suitable for hydrological models discretized by forest density at this scale, though the relationship between snow interception and snow-leaf contact area should be applicable at larger scales. Previous subcanopy snow accumulation models were developed based on process understanding at varying scales: Hedstrom & Pomeroy (1998) used snow survey transects at the forest plot scale with observations at intervals ranging from days to weeks, whilst Storck et al. (2002) relied on point-scale lysimetry observations at 30-minute intervals. Recent evidence from Staines & Pomeroy (2023) and the results presented here suggest that some of the process understanding developed in previous studies may not be applicable at larger extents or finer temporal resolutions. The theoretical basis of the vector-based model is supported by observations across a broad range of meteorological conditions and forest densities and aligns with globally tested rainfall interception models (e.g., Valante et al., 1997; Zhong et al., 2022), suggesting potential broader applicability, though further validation is required.

576 6 Conclusions

577 New observations of initial snow interception, collected over a wide range of meteorological
578 conditions and canopy densities indicate that leaf contact area is the primary factor influencing
579 subcanopy snow accumulation. At the point scale, measurements revealed no evidence of
580 a maximum canopy snow load, even for event snowfalls up to 45 mm, nor was there any
581 indication of air temperature influencing the cohesion and adhesion of snowfall to the canopy.

582 Instead, wind speed was found to influence interception efficiency by changing the hydrometeor
583 trajectory angle, which led to a substantial increase in snow-leaf contact area.

584 At the forest plot scale, UAV-lidar measurements of throughfall aligned with the point-scale
585 observations demonstrating that leaf contact area was strongly associated with interception
586 efficiency at a particular site. Leaf contact area, which incorporates changes in canopy density
587 with hydrometeor trajectory angle, proved to be a better predictor of interception efficiency
588 compared to nadir-calculated canopy cover. When averaged across each forest plot, leaf contact
589 area was shown to be highly sensitive to hydrometeor trajectory angle, increasing by 61–
590 95% for trajectory angles associated with a 1 m s^{-1} wind speed. An existing theoretical
591 relationship failed to adequately represent the measured increase in leaf contact area with
592 simulated trajectory angles. As a result, a new relationship is proposed as a function of canopy
593 cover and hydrometeor trajectory angle, approximated from wind speed and hydrometeor
594 terminal fall velocity, demonstrated accurate performance at this study site.

595 The weak association between air temperature and canopy snow load with initial interception
596 efficiency, as presented here and in earlier studies, coupled with novel insights on the influence
597 of wind speed on leaf contact area, suggests the potential benefits of a new snow interception
598 parameterisation. A new parameterisation is proposed that calculates initial interception as
599 a function of snowfall and leaf contact area. This parameterisation is consistent with rainfall
600 interception studies, which also separate canopy loading and ablation processes, and calculate
601 interception as a function of canopy cover. Additionally, a second equation is proposed to
602 estimate leaf contact area as a function of hydrometeor trajectory angle and nadir canopy

603 cover. This updated snow interception parameterisation performed well in the subalpine forest
604 studied here at the forest plot scale. However, further validation is necessary in a range of
605 climates, forests, and spatial extents.

606 **7 Acknowledgments**

607 We acknowledge financial support from the University of Saskatchewan Dean's Scholarship,
608 the Natural Sciences and Engineering Research Council of Canada's Discovery Grants, the
609 Canada First Research Excellence Fund's Global Water Futures Programme, Environment and
610 Climate Change Canada, Alberta Innovates Water Innovation Program, the Canada Founda-
611 tion for Innovation's Global Water Futures Observatories facility, and the Canada Research
612 Chairs Programme. We thank Madison Harasyn, Hannah Koslowsky, Kieran Lehan, Lindsey
613 Langs and Fortress Mountain Resort for their help in the field. Jacob Staines, Madison Ha-
614 rasyn, Alistair Wallace, and Rob White contributed to developing the UAV-lidar processing
615 workflow.

616 **8 Data Availability**

617 The data that support the findings in this study are available at <https://doi.org/10.5281/zenodo.14018893>.

618 **References**

- 619 Andreadis, K. M., Storck, P., & Lettenmaier, D. P. (2009). Modeling snow accumulation
620 and ablation processes in forested environments. *Water Resources Research*, 45(5), 1–33.
621 <https://doi.org/10.1029/2008WR007042>
- 622 Calder, I. R. (1990). *Evaporation in the uplands* (p. 148). Wiley.
- 623 Cebulski, A. C., & Pomeroy, J. W. (2025). Theoretical Underpinnings of Snow Interception
624 and Canopy Snow Ablation Parameterisations. *WIREs Water*, 12(e70010). <https://doi.or>
625 [g/10.1002/wat2.70010](https://doi.org/10.1002/wat2.70010)
- 626 Chianucci, F., & Macek, M. (2023). hemispheR: An R package for fisheye canopy image
627 analysis. *Agricultural and Forest Meteorology*.
- 628 Cionco, R. M. (1965). A mathematical model for air flow in a vegetative canopy. *Journal of
629 Applied Meteorology* (1962), 4(4), 517–522. [https://doi.org/10.1175/1520-0450\(1965\)004](https://doi.org/10.1175/1520-0450(1965)004)
630 [%3C0517:AMMFAF%3E2.0.CO;2](https://doi.org/10.1175/1520-0450(1965)004-0517:AMMFAF%3E2.0.CO;2)
- 631 Clark, M. P., Nijssen, B., Lundquist, J. D., Kavetski, D., Rupp, D. E., Woods, R. A., Freer,
632 J. E., Gutmann, E. D., Wood, A. W., Gochis, D. J., Rasmussen, R. M., Tarboton, D. G.,
633 Mahat, V., Flerchinger, G. N., & Marks, D. G. (2015). A unified approach for process-
634 based hydrologic modeling: 2. Model implementation and case studies. *Water Resources
635 Research*, 51(4), 2515–2542. <https://doi.org/10.1002/2015WR017200>
- 636 Ellis, C. R., Pomeroy, J. W., Brown, T., & MacDonald, J. (2010). Simulation of snow accumu-
637 lation and melt in needleleaf forest environments. *Hydrology and Earth System Sciences*,
638 14(6), 925–940. <https://doi.org/10.5194/hess-14-925-2010>
- 639 Ellis, C. R., Pomeroy, J. W., & Link, T. E. (2013). Modeling increases in snowmelt yield and
640 desynchronization resulting from forest gap-thinning treatments in a northern mountain
641 headwater basin. *Water Resources Research*, 49(2), 936–949. <https://doi.org/10.1002/wr>
642 [cr.20089](https://doi.org/10.1002/wr.20089)
- 643 Essery, R., Pomeroy, J. W., Parviainen, J., & Storck, P. (2003). Sublimation of snow from
644 coniferous forests in a climate model. *Journal of Climate*, 16(11), 1855–1864. [https://doi.org/10.1175/1520-0442\(2003\)016%3C1855:SOSFCF%3E2.0.CO;2](https://doi.org/10.1175/1520-0442(2003)016%3C1855:SOSFCF%3E2.0.CO;2)

- 646 Floyd, W. C. (2012). *Snowmelt energy flux recovery during rain-on-snow in regenerating*
647 *forests* (p. 180) [MSc. Thesis, University of British Columbia]. <https://doi.org/https://dx.doi.org/10.14288/1.0073024>
- 649 Fryer, B. Y. G. I., Johnson, E. A., Fryer, G. I., & Johnson, E. A. (1988). Reconstructing
650 fire behaviour and effects in a subalpine forest. *The Journal of Applied Ecology*, 25(3),
651 1063–1072. <https://doi.org/10.2307/2403766>
- 652 Gelfan, A. N., Pomeroy, J. W., & Kuchment, L. S. (2004). Modeling forest cover influences on
653 snow accumulation, sublimation, and melt. *Journal of Hydrometeorology*, 5(5), 785–803.
654 [https://doi.org/10.1175/1525-7541\(2004\)005%3C0785:MFCIOS%3E2.0.CO;2](https://doi.org/10.1175/1525-7541(2004)005%3C0785:MFCIOS%3E2.0.CO;2)
- 655 Golding, D. L., & Swanson, R. H. (1978). Snow accumulation and melt in small forest openings
656 in Alberta. *Canadian Journal of Forest Research*, 8(4), 380–388. <https://doi.org/10.1139/x78-057>
- 658 Harder, P., & Pomeroy, J. W. (2013). Estimating precipitation phase using a psychrometric
659 energy balance method. *Hydrological Processes*, 27(13), 1901–1914. <https://doi.org/10.1002/hyp.9799>
- 661 Harder, P., Pomeroy, J. W., & Helgason, W. D. (2020). Improving sub-canopy snow depth
662 mapping with unmanned aerial vehicles: Lidar versus structure-from-motion techniques.
663 *The Cryosphere*, 14(6), 1919–1935. <https://doi.org/10.5194/tc-14-1919-2020>
- 664 Harpold, A. A., Krogh, S. A., Kohler, M., Eckberg, D., Greenberg, J., Sterle, G., & Broxton,
665 P. D. (2020). Increasing the efficacy of forest thinning for snow using high-resolution
666 modeling: A proof of concept in the Lake Tahoe Basin, California, USA. *Ecohydrology :
667 Ecosystems, Land and Water Process Interactions, Ecohydrogeomorphology*, 13(4). <https://doi.org/10.1002/eco.2203>
- 669 Hedstrom, N. R., & Pomeroy, J. W. (1998). Measurements and modelling of snow interception
670 in the boreal forest. *Hydrological Processes*, 12(10-11), 1611–1625. [https://doi.org/10.1002/\(SICI\)1099-1085\(199808/09\)12:10/11%3C1611::AID-HYP684%3E3.0.CO;2-4](https://doi.org/10.1002/(SICI)1099-1085(199808/09)12:10/11%3C1611::AID-HYP684%3E3.0.CO;2-4)
- 672 Herwitz, S. R., & Slye, R. E. (1995). Three-dimensional modeling of canopy tree interception
673 of wind-driven rainfall. *Journal of Hydrology*, 168(1-4), 205–226. [https://doi.org/10.1016/0022-1694\(94\)02643-P](https://doi.org/10.1016/0022-1694(94)02643-P)

- 675 Isyumov, N. (1971). *An approach to the prediction of snow loads* [PhD thesis]. The University
676 of Western Ontario (Canada).
- 677 Katsushima, T., Kato, A., Aiura, H., Nanko, K., Suzuki, S., Takeuchi, Y., & Murakami, S.
678 (2023). Modelling of snow interception on a Japanese cedar canopy based on weighing
679 tree experiment in a warm winter region. *Hydrological Processes*, 37(6), 1–16. <https://doi.org/10.1002/hyp.14922>
- 680 Kim, E., Gatebe, C., Hall, D., Newlin, J., Misakonis, A., Elder, K., Marshall, H. P., Hiem-
681 stra, C., Brucker, L., De Marco, E., Crawford, C., Kang, D. H., & Entin, J. (2017).
682 NASA's snowex campaign: Observing seasonal snow in a forested environment. *2017
683 IEEE International Geoscience and Remote Sensing Symposium (IGARSS)*, 1388–1390.
684 <https://doi.org/10.1109/IGARSS.2017.8127222>
- 685 Kobayashi, D. (1987). Snow accumulation on a narrow board. *Cold Regions Science and
686 Technology*, 13(3), 239–245. [https://doi.org/10.1016/0165-232X\(87\)90005-X](https://doi.org/10.1016/0165-232X(87)90005-X)
- 687 Kozak, A., & Kozak, R. A. (1995). Notes on regression through the origin. *Forestry Chronicle*,
688 71(3), 326–330. <https://doi.org/10.5558/tfc71326-3>
- 689 Langs, L. E., Petrone, R. M., & Pomeroy, J. W. (2020). A $\delta^{18}\text{O}$ and $\delta^2\text{H}$ stable water
690 isotope analysis of subalpine forest water sources under seasonal and hydrological stress
691 in the Canadian Rocky Mountains. *Hydrological Processes*, 34(26), 5642–5658. <https://doi.org/10.1002/hyp.13986>
- 692 Lumbrazo, C., Bennett, A., Currier, W. R., Nijssen, B., & Lundquist, J. (2022). Evalu-
693 uating multiple canopy-snow unloading parameterizations in SUMMA with time-lapse
694 photography characterized by citizen scientists. *Water Resources Research*, 58(6), 1–22.
695 <https://doi.org/10.1029/2021WR030852>
- 696 Lundberg, A., & Halldin, S. (1994). Evaporation of intercepted snow: Analysis of governing
697 factors. *Water Resources Research*, 30(9), 2587–2598.
- 698 Lundquist, J. D., Dickerson-Lange, S., Gutmann, E., Jonas, T., Lumbrazo, C., & Reynolds, D.
699 (2021). Snow interception modelling: Isolated observations have led to many land surface
700 models lacking appropriate temperature sensitivities. *Hydrological Processes*, 35(7), 1–20.
701 <https://doi.org/10.1002/hyp.14274>

- 704 MacDonald, J. P. (2010). *Unloading of intercepted snow in conifer forests* (p. 93) [MSc.
705 Thesis]. Department of Geography, University of Saskatchewan.
- 706 Mazzotti, G., Currier, W. R., Deems, J. S., Pfugl, J. M., Lundquist, J. D., & Jonas, T. (2019).
707 Revisiting snow cover variability and canopy structure within forest stands: Insights from
708 airborne lidar data. *Water Resources Research*, 55(7), 6198–6216. <https://doi.org/10.1029/2019WR024898>
- 710 Moeser, D., Morsdorf, F., & Jonas, T. (2015a). Novel forest structure metrics from airborne Li-
711 DAR data for improved snow interception estimation. *Agricultural and Forest Meteorology*,
712 208, 40–49. <https://doi.org/10.1016/j.agrformet.2015.04.013>
- 713 Moeser, D., Stähli, M., & Jonas, T. (2015b). Improved snow interception modeling using
714 canopy parameters derived from airborne LiDAR data. *Water Resources Research*, 51(7),
715 5041–5059. <https://doi.org/10.1002/2014WR016724>
- 716 Musselman, K. N., Pomeroy, J. W., & Link, T. E. (2015). Variability in shortwave irradiance
717 caused by forest gaps: Measurements, modelling, and implications for snow energetics.
718 *Agricultural and Forest Meteorology*, 207, 69–82. <https://doi.org/10.1016/j.agrformet.2015.03.014>
- 720 Parviainen, J., & Pomeroy, J. W. (2000). Multiple-scale modelling of forest snow sublimation:
721 Initial findings. *Hydrological Processes*, 14(15), 2669–2681. [https://doi.org/10.1002/1099-1085\(20001030\)14:15%3C2669::AID-HYP85%3E3.0.CO;2-Q](https://doi.org/10.1002/1099-1085(20001030)14:15%3C2669::AID-HYP85%3E3.0.CO;2-Q)
- 723 Pfister, R., & Schneebeli, M. (1999). Snow accumulation on boards of different sizes and
724 shapes. *Hydrological Processes*, 13(14-15), 2345–2355. [https://doi.org/10.1002/\(SICI\)1099-1085\(199910\)13:14/15%3C2345::AID-HYP873%3E3.0.CO;2-N](https://doi.org/10.1002/(SICI)1099-1085(199910)13:14/15%3C2345::AID-HYP873%3E3.0.CO;2-N)
- 726 Pomeroy, J. W., Brown, T., Fang, X., Shook, K. R., Pradhananga, D., Armstrong, R., Harder,
727 P., Marsh, C., Costa, D., Krogh, S. A., Aubry-Wake, C., Annand, H., Lawford, P., He,
728 Z., Kompanizare, M., & Moreno, J. I. L. (2022). The cold regions hydrological modelling
729 platform for hydrological diagnosis and prediction based on process understanding. *Journal
730 of Hydrology*, 615(128711), 1–25. <https://doi.org/10.1016/j.jhydrol.2022.128711>
- 731 Pomeroy, J. W., Fang, X., & Ellis, C. R. (2012). Sensitivity of snowmelt hydrology in Marmot
732 Creek, Alberta, to forest cover disturbance. *Hydrological Processes*, 26(12), 1891–1904.

- 733 <https://doi.org/10.1002/hyp.9248>
- 734 Pomeroy, J. W., Marsh, P., & Gray, D. M. (1997). Application of a distributed blowing snow
735 model to the arctic. *Hydrological Processes*, 11(11), 1451–1464. [https://doi.org/10.1002/\(SICI\)1099-1085\(199709\)11:11%3C1451::aid-hyp449%3E3.0.co;2-q](https://doi.org/10.1002/(SICI)1099-1085(199709)11:11%3C1451::aid-hyp449%3E3.0.co;2-q)
- 736 Pomeroy, J. W., Parviainen, J., Hedstrom, N., & Gray, D. M. (1998). Coupled modelling of
737 forest snow interception and sublimation. *Hydrological Processes*, 12(15), 2317–2337. [https://doi.org/10.1002/\(SICI\)1099-1085\(199812\)12:15%3C2317::AID-HYP799%3E3.0.CO;2-X](https://doi.org/10.1002/(SICI)1099-1085(199812)12:15%3C2317::AID-HYP799%3E3.0.CO;2-X)
- 738 Pomeroy, J. W., & Schmidt, R. A. (1993). The use of fractal geometry in modelling intercepted
739 snow accumulation and sublimation. *Eastern Snow Conference*, 50, 231–239.
- 740 Pomeroy, J. W., & Schmidt, R. A. (1993). The use of fractal geometry in modelling intercepted
741 snow accumulation and sublimation. *Eastern Snow Conference*, 50, 231–239.
- 742 R Core Team. (2024). *R: A language and environment for statistical computing* [Manual]. R
743 Foundation for Statistical Computing.
- 744 Rittger, K., Raleigh, M. S., Dozier, J., Hill, A. F., Lutz, J. A., & Painter, T. H. (2020). Canopy
745 adjustment and improved cloud detection for remotely sensed snow cover mapping. *Water
746 Resources Research*, 56(6), n/a. <https://doi.org/10.1029/2019WR024914>
- 747 Roesch, A., Wild, M., Gilgen, H., & Ohmura, A. (2001). A new snow cover fraction parame-
748 terization for the ECHAM4 GCM. *Climate Dynamics*, 17(12), 933–946. <https://doi.org/10.1007/s003820100153>
- 749 Roth, T. R., & Nolin, A. W. (2019). Characterizing maritime snow canopy interception in
750 forested mountains. *Water Resources Research*, 55(6), 4564–4581. <https://doi.org/10.1029/2018WR024089>
- 751 Safa, H., Krogh, S. A., Greenberg, J., Kostadinov, T. S., & Harpold, A. A. (2021). Unraveling
752 the controls on snow disappearance in montane conifer forests using multi-site lidar. *Water
753 Resources Research*, 57(12), 1–20. <https://doi.org/10.1029/2020WR027522>
- 754 Sanmiguel-Vallelado, A., McPhee, J., Esmeralda Ojeda Carreño, P., Morán-Tejeda, E., Julio
755 Camarero, J., & López-Moreno, J. I. (2022). Sensitivity of forest–snow interactions to
756 climate forcing: Local variability in a Pyrenean valley. *Journal of Hydrology*, 605. <https://doi.org/10.1016/j.jhydrol.2021.127311>
- 757 Satterlund, D. R., & Haupt, H. F. (1967). Snow catch by conifer crowns. *Water Resources
758 Research*, 3(4), 1035–1039. <https://doi.org/10.1029/WR003i004p01035>

- 762 Schmidt, R. A., & Gluns, D. R. (1991). Snowfall interception on branches of three conifer
763 species. *Canadian Journal of Forest Research*, 21(8), 1262–1269. <https://doi.org/10.1139/x91-176>
- 765 Schmidt, R. A., & Pomeroy, J. W. (1990). Bending of a conifer branch at subfreezing temper-
766 atures: Implications for snow interception. *Canadian Journal of Forest Research*, 20(8),
767 1251–1253. <https://doi.org/10.1139/x90-165>
- 768 Schmidt, R. A., & Troendle, C. A. (1989). Snowfall into a forest and clearing. *Journal of
769 Hydrology*, 110(3-4), 335–348. [https://doi.org/10.1016/0022-1694\(89\)90196-0](https://doi.org/10.1016/0022-1694(89)90196-0)
- 770 Smith, C. D. (2007). Correcting the wind bias in snowfall measurements made with a Geonor
771 T-200B precipitation gauge and alter wind shield. *87th AMS Annual Meeting*.
- 772 Staines, J., & Pomeroy, J. W. (2023). Influence of forest canopy structure and wind flow
773 on patterns of sub-canopy snow accumulation in montane needleleaf forests. *Hydrological
774 Processes*, 37(10), 1–19. <https://doi.org/10.1002/hyp.15005>
- 775 Storck, P., Lettenmaier, D. P., & Bolton, S. M. (2002). Measurement of snow interception and
776 canopy effects on snow accumulation and melt in a mountainous maritime climate, Oregon,
777 United States. *Water Resources Research*, 38(11), 1–16. <https://doi.org/10.1029/2002wr001281>
- 779 Troendle, C. A. (1983). The potential for water yield augmentation from forest management
780 in the rocky mountain region. *Journal of the American Water Resources Association*, 19(3),
781 359–373. <https://doi.org/10.1111/j.1752-1688.1983.tb04593.x>
- 782 Valante, F., David, J. S., & Gash, J. H. C. (1997). Modelling interception loss for two sparse
783 eucalypt and pine forests in central Portugal using reformulated Rutter and Gash analytical
784 models. *Journal of Hydrology*, 190(1-2), 141–162. [https://doi.org/10.1016/S0022-1694\(96\)03066-1](https://doi.org/10.1016/S0022-1694(96)03066-1)
- 786 Van Stan, J. T., Siegert, C. M., Levia, D. F., & Scheick, C. E. (2011). Effects of wind-
787 driven rainfall on stemflow generation between codominant tree species with differing crown
788 characteristics. *Agricultural and Forest Meteorology*, 151(9), 1277–1286. <https://doi.org/10.1016/j.agrformet.2011.05.008>
- 790 Varhola, A., Coops, N. C., Weiler, M., & Moore, R. D. (2010). Forest canopy effects on

- 791 snow accumulation and ablation: An integrative review of empirical results. *Journal of*
792 *Hydrology*, 392(3-4), 219–233. <https://doi.org/10.1016/j.jhydrol.2010.08.009>
- 793 Vionnet, V., Mortimer, C., Brady, M., Arnal, L., & Brown, R. (2021). Canadian historical
794 snow water equivalent dataset (CanSWE, 1928–2020). *Earth System Science Data*, 13(9),
795 4603–4619. <https://doi.org/10.5194/essd-13-4603-2021>
- 796 Watanabe, S., & Ozeki, J. (1964). Study of fallen snow on forest trees (II). Experiment on the
797 snow crown of the Japanese cedar. *Japanese Govt. Forest Exp. Sta. Bull*, 169, 121–140.
- 798 Zhong, F., Jiang, S., van Dijk, A. I. J. M., Ren, L., Schellekens, J., & Miralles, D. G.
799 (2022). Revisiting large-scale interception patterns constrained by a synthesis of global
800 experimental data. *Hydrology and Earth System Sciences*, 26(21), 5647–5667. <https://doi.org/10.5194/hess-26-5647-2022>